Nucleobindin-2 consists of two structural components: The Zn²⁺-sensitive N-terminal half, consisting of nesfatin-1 and -2, and the Ca²⁺-sensitive C-terminal half, consisting of nesfatin-3

Dominika Bystranowska [a],[*],[1], Anna Skorupska [a],[1], Katarzyna Sołtys [a], Michał Padjasek [b], Artur Krężel [b], Andrzej Żak [c], Magdalena Kaus-Drobek [d], Michał Taube [e], Maciej Kozak [e],[f], Andrzej Ożyhar [a]

[a] Department of Biochemistry, Molecular Biology and Biotechnology, Faculty of Chemistry, Wrocław University of Science and Technology, Wybrzeże Wyspiańskiego 27, 50-370 Wrocław, Poland
[b] Department of Chemical Biology, Faculty of Biotechnology, University of Wrocław, Joliot-Curie 14a, 50-383 Wrocław, Poland
[c] Faculty of Mechanical Engineering, Wrocław University of Science and Technology, Wybrzeże Wyspiańskiego 27, 50-370 Wrocław, Poland
[d] Institute of Biochemistry and Biophysics, Polish Academy of Sciences, 02-106 Warsaw, Poland
[e] Department of Macromolecular Physics, Faculty of Physics, Adam Mickiewicz University, Umultowska 85, 61-614 Poznań, Poland
[f] National Synchrotron Radiation Centre SOLARIS, Jagiellonian University, Czerwone Maki 98, 30-392 Kraków, Poland

ARTICLE INFO

ABSTRACT

Nucleobindin-2 (Nucb2) is a protein that has been suggested to play roles in a variety of biological processes. Nucb2 contains two Ca²⁺/Mg²⁺-binding EF-hand domains separated by an acidic amino acid residue-rich region and a leucine zipper. All of these domains are located within the C-terminal half of the protein. At the N-terminal half, Nucb2 also possesses a putative Zn²⁺-binding motif. In our recent studies, we observed that Nucb2 underwent Ca²⁺-dependent compaction and formed a mosaic-like structure consisting of intertwined disordered and ordered regions at its C-terminal half. The aim of this study was to investigate the impact of two other potential ligands: Mg²⁺, which possesses chemical properties similar to those of Ca²⁺, and Zn²⁺, for which a putative binding motif was identified. In this study, we demonstrated that the binding of Mg²⁺ led to oligomerization state changes with no significant secondary or tertiary structural alterations of Nucb2. In contrast, Zn²⁺ binding had a more pronounced effect on the structure of Nucb2, leading to the local destabilization of its N-terminal half while also inducing changes within its C-terminal half. These structural rearrangements resulted in the oligomerization and/or aggregation of Nucb2 molecules. Taken together, the results of our previous and current research help to elucidate the structure of the Nucb2, which can be divided into two parts: the Zn²⁺-sensitive N-terminal half (consisting of nesfatin-1 and -2) and the Ca²⁺-sensitive C-terminal half (consisting of nesfatin-3). These results may also help to open a new discussion regarding the diverse roles that metal cations play in regulating the structure of Nucb2 and the various physiological functions of this protein.

1. Introduction

Metal ions have a significant impact on a variety of biological processes. In fact, these ions are essential for the functioning of approximately one-third of proteins. Metal-protein interactions are involved in the conformational alternation of the structure of proteins and the catalysis of biological processes [1]. Ca²⁺, Mg²⁺ and Zn²⁺, which are divalent metal cations, are among the most important metal ions due to their abundance in the body [2–4]. Ca²⁺, a ubiquitous secondary messenger, regulates relevant processes from cell signalling to apoptosis [5]. The most common Ca²⁺-binding motif in proteins is the EF-hand domain [6,7]. Another essential metal ion, Mg²⁺, possesses chemical properties similar to those of Ca²⁺ and is also able to bind to the EF-hand domain [6]. However, the cytosolic concentration of Mg²⁺ is approximately three orders of magnitude higher than that of Ca²⁺ [8]. Due to the different ionic radii of Mg²⁺ (0.86 Å) and Ca²⁺ (1.14 Å), proteins with EF-hand domains can differentiate Ca²⁺ from Mg²⁺ [9].

* Corresponding author.
E-mail address: dominika.bystranowska@pwr.edu.pl (D. Bystranowska).
[1] Both authors contributed equally to this work.

Zn^{2+}, one of the most abundant d-block metal ions, is essential as a cofactor for the enzymes and structural or regulatory elements of proteins [10]. Bioinformatic analysis revealed that approximately 10% of proteins in the human genome are involved in Zn^{2+} binding [11]. Unlike Ca^{2+} and Mg^{2+}, Zn^{2+} has a stronger affinity for proteins [12]. Zn^{2+} ions can bind between four to six protein ligands, such as the nitrogen atoms of His, sulfur atoms of Cys and oxygen atoms of Asp and Glu residues, and form complexes with tetrahedral to octahedral geometry [10,13]. The most classical structural Zn^{2+}-binding site is formed by the Cys2His2 coordination environment in the ββα zinc finger domain [14]. However, other structural Zn^{2+}-binding sites, such as Cys4, Cys3His, AspHis3, and His2Asp2, are also common [15,16]. Zn^{2+} is also implicated in cellular regulation [3,17]. The total Zn^{2+} concentration in eukaryotic cells is several hundred micromolar. However, the free Zn^{2+} concentration is considerably lower, being in the picomolar to sub-nanomolar range [12,18]. The concentration of Zn^{2+} must be tightly regulated, with both an abundance and deficiency of Zn^{2+} being adverse for cells [19,20]. Multiple proteins (e.g., the metallothionein family) are involved in Zn^{2+} homeostasis to keep the free Zn^{2+} concentration at the proper range and to provide this element for multiple Zn^{2+}-binding proteins [21]. Compartmentation of Zn^{2+} in different cellular organelles by Zn^{2+} transporters is also characteristic of the control of Zn^{2+} levels in eukaryotic cells [12,22]. The vesicles of neurons and pancreatic β cells are examples of organelles that store large amounts of Zn^{2+} [23,24]. The concentration of free Zn^{2+} is increased locally by the vesicular release of Zn^{2+} [25]. This Zn^{2+} increase participates in protein function regulation and controls various cellular processes implicated in signal transduction [26]. Importantly, dysregulated changes that lead to Zn^{2+} dyshomeostasis are related to several neurodegenerative diseases [27] and mental disorders, such as depression [28]. The binding of Zn^{2+} affects the aggregation kinetics and morphology of a high percentage of amyloid proteins, such as amyloid-β [29,30], Tau [31], islet amyloid polypeptide [32,33], β2-microglobulin [34] and superoxide dismutase 1 [35]. A high Zn^{2+} concentration could also lead to protein precipitation and modulate the toxicity of protein aggregates [36].

Nucleobindin-2 (Nucb2) is a multidomain protein consisting of six domains: the Ile/Leu-rich region, the DNA-binding domain (DBD), two EF-hand domains, the acidic amino acid rich region, and the leucine zipper motif [37]. Nucb2 can be proteolytically cleaved into three peptides: nesfatin-1, nesfatin-2, and nesfatin-3 [38]. Only the function of nesfatin-1 has been determined [38]. Oh-I [38] showed that nesfatin-1 is involved in food intake inhibition [38]. Nucb2 also participates in other biological processes, e.g., adipogenesis [39], biomineralization [40] and carcinogenesis [41,42]. Additionally, Nucb2 is ubiquitously expressed in the central nervous system [38] and peripheral tissues, such as the digestive tract [43], reproductive system [44], pancreas [45,46], and heart [47]. The multifunctionality of Nucb2 may result from its structure. Nucb2 possesses two EF-hand domains [37], which are able to bind Ca^{2+} and Mg^{2+} ions [6]. Additionally, Nucb2 contains a putative Zn^{2+}-binding motif at its N-terminal half, similar to its paralogue Nucb1 [48]. Our previous research showed that Nucb2s from *Gallus gallus* (ggNucb2) and *Homo sapiens* (hsNucb2) belong to the family of intrinsically disordered proteins (IDPs) [49]. We also revealed that Ca^{2+} binding affects the overall structure of Nucb2 molecules, which leads to their compaction with the simultaneous formation of a mosaic-like structure consisting of intertwined disordered and ordered regions of the initially disordered C-terminal half of apo-Nucb2 [49]. However, the impact of Mg^{2+} and Zn^{2+} on the structure of Nucb2s has not been examined to date. Therefore, the aim of this study was to characterize the structural properties of both Nucb2 homologues in the presence of Zn^{2+} and Mg^{2+} using a range of biophysical experimental approaches. In this study, we demonstrate the presence of two Zn^{2+}-binding sites and a single Mg^{2+}-binding site within Nucb2 molecules. Moreover, the results of this study indicate that Mg^{2+} or Zn^{2+} binding leads to conformational changes in the structures of both proteins. Induced by Zn^{2+} binding, destabilization of the structure of Nucb2s within the N-terminal half leads to the self-assembly of the proteins' molecules and the formation of higher oligomers. On the other hand, Mg^{2+} binding does not induce significant changes in the secondary/tertiary structure of Nucb2s. However, Mg^{2+} impacts the oligomerization state of Nucb2s, leading to the appearance of ggNucb2 dimeric species and the slightly compacted molecules of hsNucb2. The results presented in this report provide comprehensive insight into the structure of Nucb2 molecules, which appear to be divided into two parts: the Zn^{2+}-sensitive N-terminal half, consisting of nesfatin-1 and -2, and the Ca^{2+}-sensitive C-terminal half, which consists of nesfatin-3.

2. Results

2.1. Secondary structure modulation of Nucb2s revealed by CD

Previously [49], we showed that in the presence of Ca^{2+}, ggNucb2 and hsNucb2 undergo a significant compaction of their structure, including an increase in the content of the α-helical structure, while exhibiting a simultaneous decrease in the fraction of random coil regions. In this study, we examined other divalent metal ions – Zn^{2+} and Mg^{2+} – as well as their effect on Nucb2 secondary structures. In the first step, we performed far-UV CD spectra measurements of Nucb2s in the absence and presence of 100–300 μM Zn^{2+} and 10 mM Mg^{2+}. Such a concentration of Mg^{2+} was chosen due to the mM range of the physiological concentration of Mg^{2+} [4]. The estimates of the total intracellular Mg^{2+} concentration are 15 mM, whereas the ionized intracellular Mg^{2+} concentration ranges between 0.5 and 1.0 mM [50]. We decided to use a μM Zn^{2+} concentration because Zn^{2+} within the μM range can accumulate in a variety of cells and tissues, e.g., neurons [51] and pancreatic β-cells [52], under physiological conditions, despite the low free Zn^{2+} concentration (pM to nM range). Additionally, pathological states are also related to the accumulation of Zn^{2+} at μM concentrations [53,54]. As shown in Fig. 1A and 1B, the CD spectra of both apo-Nucb2s show typical negative maxima for the α-helical structure at 208 nm and 222 nm [55]. These results were supported by deconvolution of CD data using CDNN software [56], which shows that Nucb2s consist primarily of the α-helical structure (ggNucb2 – 45.10 ± 0.01%, hsNucb2 – 55.60 ± 0.27%, see Table 1). The analysis also indicated the presence of a significant number of random coil regions (ggNucb2 – 25.60 ± 1.5%, hsNucb2 – 20.3 ± 0.2%). The presence of 100 μM and 200 μM Zn^{2+} was observed to slightly modulate the secondary structure composition of Nucb2s, leading to an increase in the α-helical structure content and a decrease in the random coil content (Table 1 and Fig. 1A and B). Notably, incubation of ggNucb2 with 300 μM Zn^{2+} caused the CD signal to decay (Fig. 1A). Conversely, the addition of 300 μM Zn^{2+} had a similar effect on the structure of hsNucb2 as the addition of 200 μM Zn^{2+} (Fig. 1B). At the protein concentration that was employed and with increasing concentrations of Zn^{2+} (≥300 μM), the measurements performed for ggNucb2 were observed to be more problematic due to the precipitation of the protein compared with the measurements performed for hsNucb2. On the other hand, Mg^{2+} had no impact on the secondary structure of ggNucb2. The spectra of ggNucb2 in the absence and presence of 10 mM Mg^{2+} were determined to be superimposable (see Fig. 1A). Mg^{2+} affected, however, the secondary structure of hsNucb2. The deconvoluted CD spectra showed that the effect of Mg^{2+} on the secondary structure of hsNucb2 was similar to the effect of 100 μM
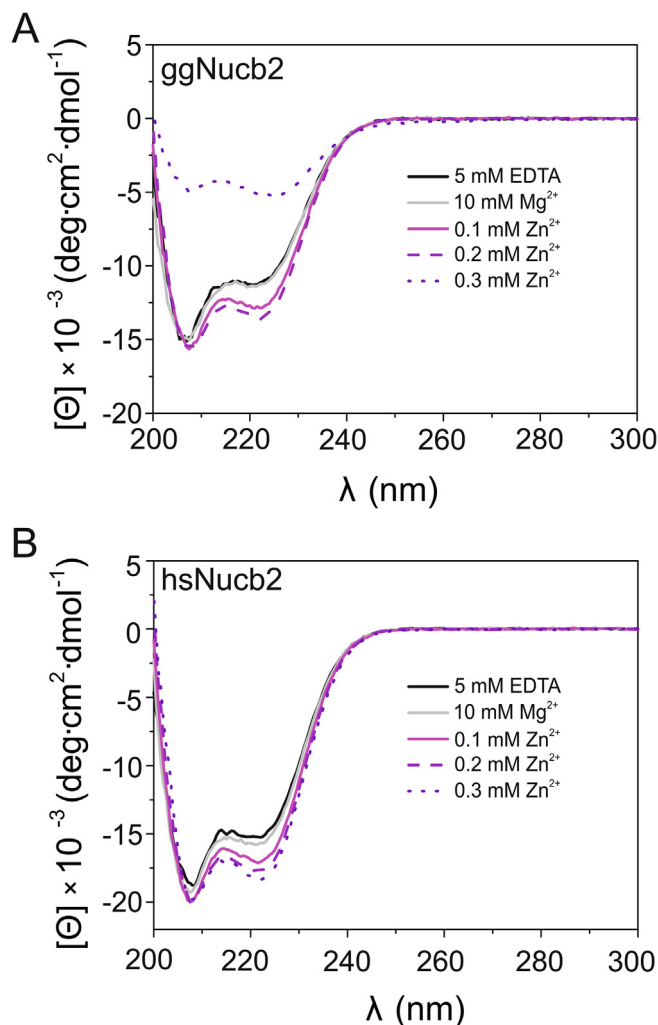
Fig. 1. Effect of Zn^{2+} and Mg^{2+} on the secondary structure of Nucb2s. (A) Far-UV CD spectra of ggNucb2 (10 µM) in buffer C in the presence of 5 mM EDTA (solid black line), in the presence of 10 mM $MgCl_2$ (solid grey line), in the presence of 100 µM $ZnCl_2$ (solid magenta line), in the presence of 200 µM $ZnCl_2$ (dashed purple line), and in the presence of 300 µM $ZnCl_2$ (dotted violet line). (B) Far-UV CD spectra of hsNucb2 (10 µM) in buffer C in the presence of 5 mM EDTA (solid black line), in the presence of 10 mM $MgCl_2$ (solid grey line), in the presence of 100 µM $ZnCl_2$ (solid magenta line), in the presence of 200 µM $ZnCl_2$ (dashed purple line), and in the presence of 300 µM $ZnCl_2$ (dotted violet line). The data shown are representative of three independent experiments. (For interpretation of the references to colour in this figure legend, the reader is referred to the web version of this article.)

Zn^{2+}, as addition of both cations induced a slight increase in the α-helical structure content of hsNucb2 (Fig. 1B and Table 1).

2.2. Tertiary structure change of holo-Nucb2s revealed by fluorescence spectroscopy

CD spectra analysis revealed that Zn^{2+} slightly modified the secondary structure of Nucb2s, thereby leading to an increase in the α-helical content. To investigate possible changes in the tertiary structure, we utilized the intrinsic fluorescence of Trp residues. The emission spectrum of Trp residues depends on the polarity of their environment [57]. The two Trp residues present in the structure of both Nucb2 molecules were determined to be fully exposed to the solvent in the absence of metal cations, since the emission maxima were observed at 355 nm and 357 nm for ggNucb2 and hsNucb2, respectively (Fig. 2A, Fig. 2B). This property is characteristic of Trp residues located within the inherently disordered regions (IDRs) of proteins [57]. The addition of 100–300 µM $ZnCl_2$, however, led to a visible blueshift of the fluorescence maxima of 10 nm (to 345 nm and 347 nm for ggNucb2 and hsNucb2, respectively), suggesting that the polarity of the microenvironment of the Trp residues changed to become more hydrophobic after Zn^{2+} binding (see Fig. 2A and 2B). Additionally, the fluorescence intensity of the Trp residues of ggNucb2 in the presence of 300 µM Zn^{2+} decreased, which might also be attributable to the precipitation of protein. Notably, the presence of Mg^{2+} has no impact on the position of the Trp emission maxima of Nucb2s. These data indicate that the presence of Zn^{2+} impacts the tertiary structure of both Nucb2s, which can be explained by the notable structural rearrangement of the corresponding regions, which probably leads to the compaction of the protein molecules.

2.3. Nucb2 quaternary structure changes induced by divalent metal cations observed by SV-AUC

We recently reported [49] that Nucb2s exist in solution as extended molecules with the propensity for dimerization and simultaneous compaction induced by Ca^{2+} binding. These flexible characteristics of the Nucb2 structure were thought to play important roles in the variety of Ca^{2+}-dependent interactions with different protein partners [58,59]. In this study, we investigated how the conformation of Nucb2 molecules changes upon binding Zn^{2+} and Mg^{2+} and whether these divalent metal cations influence the quaternary structure of Nucb2. Using SV-AUC, we observed that the sedimentation profiles of Nucb2s fit a continuous c(s) distribution model and that major peaks of $s_{(20,w)} = 3.08$ S and $s_{(20,w)} = 3.39$ S (Table 2) were observed at the highest protein concentration and
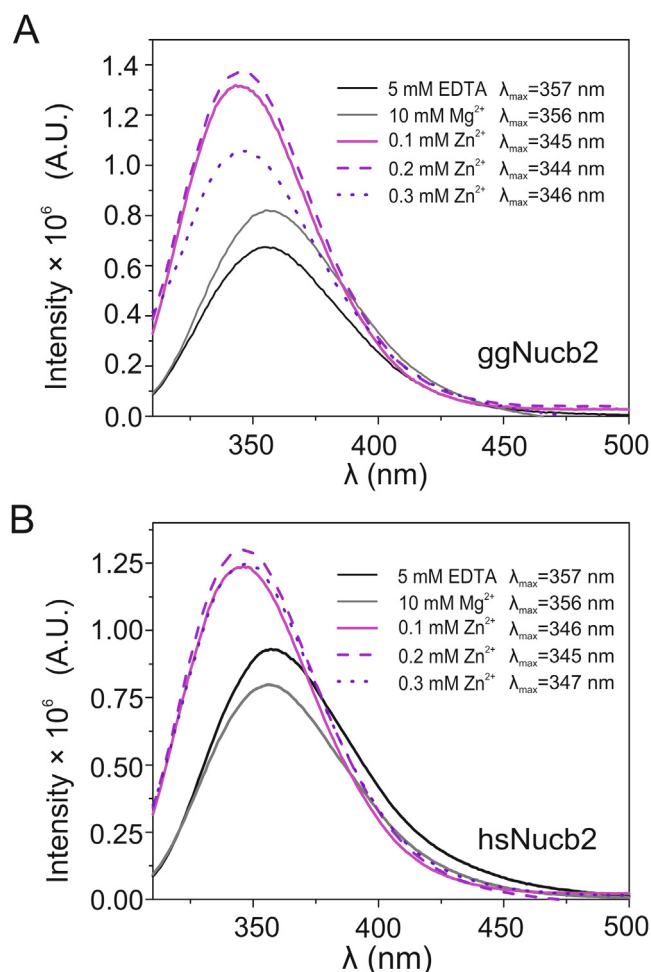
Table 1
Secondary structure composition of Nucb2s in the absence and presence of Zn^{2+} and Mg^{2+}. The table shows the content (%) of each secondary structural element in the Nucb2s estimated by CDNN [56]. The results collected for ggNucb2 in the presence of 300 µM Zn^{2+} (*) do not sum to 100% and should be treated with caution due to partial protein precipitation. The results are the average of three independent experiments.

Agent	α-helix	Antiparallel β-sheet	Parallel β-sheet	β-turn	Random coil
	[%]				
ggNucb2					
5 mM EDTA	45.1 ± 0.0	5.7 ± 0.0	6.3 ± 0.3	15.1 ± 0.0	25.6 ± 1.5
100 µM $ZnCl_2$	49.8 ± 0.5	5.2 ± 0.1	5.5 ± 0.1	14.4 ± 0.1	23.2 ± 0.3
200 µM $ZnCl_2$	51.7 ± 0.8	4.9 ± 0.1	5.2 ± 0.1	14.1 ± 0.1	22.3 ± 0.4
300 µM $ZnCl_2$*	18.7 ± 0.0	12.6 ± 0.0	15.4 ± 0.1	19.7 ± 0.0	46.6 ± 0.0
10 mM $MgCl_2$	43.5 ± 2.0	6.0 ± 0.3	6.6 ± 0.4	15.3 ± 0.3	26.5 ± 1.2
hsNucb2					
5 mM EDTA	55.6 ± 0.3	4.4 ± 0.0	4.6 ± 0.1	13.7 ± 0.0	20.3 ± 0.2
100 µM $ZnCl_2$	60.5 ± 0.2	3.9 ± 0.6	3.9 ± 0.6	13.0 ± 0.6	18.0 ± 0.6
200 µM $ZnCl_2$	62.4 ± 0.5	3.7 ± 0.6	3.7 ± 0.1	12.8 ± 0.6	17.2 ± 0.2
300 µM $ZnCl_2$	62.8 ± 0.3	3.6 ± 0.0	3.7 ± 0.1	12.7 ± 0.1	17.2 ± 0.2
10 mM $MgCl_2$	59.4 ± 0.6	4.0 ± 0.0	4.1 ± 0.0	13.2 ± 0.0	18.5 ± 0.0

Fig. 2. Intrinsic fluorescence spectra of Nucb2s in the presence of 5 mM EDTA and 10 mM Mg^{2+} and in the presence of an increasing concentration of Zn^{2+} (100–300 μM). The fluorescence spectra of (A) ggNucb2 and (B) hsNucb2. The protein concentration was 2 μM. The measurements were performed at 20 °C.

in the absence of metal cations, respectively. The major population of molecules in all the analysed samples of apo-ggNucb2 (Fig. 3) existed as monomers (apparent molecular mass, MMapp, of 51 kDa at the lowest protein concentration, which was in good agreement with the theoretical MM of 51.4 kDa). However, instead of one peak for the lowest apo-ggNucb2 concentration (Fig. 3A, B), two better-resolved peaks were detected with an increasing protein concentration (Fig. 3C-F), each of which could presumably be composed of one or more different components that undergo rapid and reversible association.

In the presence of 100 μM Zn^{2+} and 10 mM Mg^{2+}, ggNucb2 was observed as a mixture of different species. A small fraction of ggNucb2 dimers (or trimers) was detected in the presence of Mg^{2+} (Table 2), suggesting that the binding of Mg^{2+} may influence the stability of the dimeric form. The most pronounced differences between the apo- and holo-states of ggNucb2 were observed after the addition of Zn^{2+} (Fig. 3A, C, E), where the major peaks appeared to be less prominent and considerably broader than those of the apo-protein samples. Zn^{2+}-dependent association was not only manifested by ggNucb2s dimerization. We also observed the formation of higher-molecular-weight oligomers and an overall increase in the population of ggNucb2 conformations (Table 2). Moreover, the addition of Zn^{2+} up to a concentration of 300 μM caused a visible precipitation of ggNucb2 (each time when the protein concentration was ≤0.5 mg/ml), which we removed by exten-

sive centrifugation prior to loading the cell (Fig. S1). The remaining soluble protein was still highly aggregated, indicating that Zn^{2+} induces oligomerization and the formation of large aggregates of ggNucb2s in solution.

In contrast, apo-hsNucb2 mostly existed in the dimeric state in solution (theoretical MM of the monomer: 47.7 kDa). A similar oligomerization state of hsNucb2 was observed in the presence of Mg^{2+} (Fig. 4B, D, F). On the other hand, in the presence of $ZnCl_2$ (Fig. 4A, C, E), the amount of monomeric fractions increased (Table 2).

The AUC experiments revealed not only that the oligomerization state of the Nucb2s was changed in the presence of metal cations but also that the shape of both proteins changed. According to the collected data, apo-ggNucb2 turned out to be more compact than apo-hsNucb2 (frictional ratio – f/f_0 of 1.76 and 2.07, respectively). An additional significant change in the f/f_0 values was observed after Zn^{2+} binding. The f/f_0 value decreased comparably for both proteins (Table 2), especially at a protein concentration of 0.5 mg/ml, indicating a conformational change to a more compact or more globular-like structure. In the presence of Mg^{2+}, the f/f_0 value of ggNucb2 remained the same compared to the apo-state of the protein, indicating no changes in the global conformation induced by this ligand. Simultaneously, for Mg^{2+}-saturated hsNucb2, a small decrease in the f/f_0 and R_h values compared to the apo state was observed. Additionally, the obtained results showed small concentration-dependent changes in the f/f_0 values (the change from 1.74 to 1.89 with the concentration change ranging from 0.5 to 1.0 mg/ml) for holo-hsNucb2 after Mg^{2+} binding.

Based on the hydrodynamic properties determined by AUC, we can conclude that Nucb2s exist in solution as extended molecules, of which both the shape and the oligomerization state changed in the presence of metal cations, though in a different way for each of the homologues. The overall conformation of Mg^{2+}-bound ggNucb2 seemed to be similar to the conformation of apo-ggNucb2 to a greater degree than that observed for hsNucb2 which, in turn, became more compact, especially at lower protein concentrations. On the other hand, observations made for Nucb2s saturated with Zn^{2+} suggested that not only oligomerization but also metal ion-driven aggregation processes could occur in the samples. Such aggregation may lead, in turn, to the formation of multiple extended protein conformations. This behaviour, to which ggNucb2 samples are considerably more vulnerable, is at the same time accompanied by protein precipitation at a specific Zn^{2+}-to-protein molar ratio.

2.4. Thermodynamics of the interactions of Nucb2 with divalent metal ions

Fluorescence spectroscopy and AUC showed that Nucb2s in the presence of Zn^{2+} undergo tertiary and quaternary structural changes. On the other hand, Mg^{2+} has an effect on the oligomerization state of Nucb2s without significant secondary and tertiary structure changes. ITC measurements were performed to elucidate the thermodynamic parameters of Nucb2-Zn^{2+} and Nucb2-Mg^{2+} interactions.

The first set of experiments focused on Zn^{2+} binding analysis. The binding of Zn^{2+} to ggNucb2 is represented by a complex thermogram that encompasses both exo- and endothermic processes (Fig. 5A). To further characterize additional equilibria, Zn^{2+} titration was performed with 1000 and 4000 μM titrant concentrations in a syringe (Fig. 5A, Fig. S2). The first experiment illuminated a gradually increasing exothermic process that may correspond with ligand-mediated dimerization. The second experiment, which employed the higher titrant concentration, demonstrated the contribution of the endothermic process that coincided with the first reaction, presenting higher absolute values of measured heats

Table 2
Hydrodynamic properties of the Nucb2s.

Protein	Agent	c [mg/ml]	rmsd	$s_{(20,w)}$ [S]	f/f_0	R_h [nm]	MM_{app} [kDa]
ggNucb2	EDTA	0.5	0.005871	2.89	1.75	4.28	51 (100%)
		0.75	0.006157	2.46	1.75	3.99	41 (20%)
				3.04		4.43	56 (80%)
		1.0	0.006470	2.42	1.76	3.97	40 (20%)
				3.08		4.48	57 (80%)
	MgCl$_2$	0.5	0.005721	3.09	1.74	4.42	57 (93%)
				5.69		6.00	142 (7%)
		0.75	0.006160	2.78	1.74	4.20	49 (26%)
				3.31		4.58	63 (67%)
				5.61		5.97	139 (7%)
		1.0	0.006452	2.74	1.76	4.23	48 (21%)
				3.35		4.68	65 (73%)
				5.72		6.12	145 (6%)
	ZnCl$_2$	0.5	0.005836	3.53	1.23	2.79	41 (88%)
				8.60		4.36	156 (12%)
		0.75	0.006141	3.24	1.40	3.27	44 (37%)
				3.93		3.61	59 (50%)
				6.19		4.52	116 (3%)
				8.88		5.42	200 (10%)
		1.0	0.006762	3.05	1.58	3.78	48 (35%)
				3.61		4.11	61 (52%)
				5.74		5.19	124 (5%)
				7.74		6.03	194 (8%)
hsNucb2	EDTA	0.5	0.005929	2.50	2.07	5.21	55 (4%)
				3.37		6.06	86 (96%)
		0.75	0.006217	2.42	2.04	5.02	51 (3%)
				3.38		5.94	85 (97%)
		1.0	0.007139	2.41	2.07	5.15	52 (1%)
				3.39		6.10	87 (99%)
	MgCl$_2$	0.5	0.005852	2.76	1.74	4.23	49 (10%)
				3.55		4.81	72 (90%)
		0.75	0.006220	2.71	1.83	4.49	51 (7%)
				3.56		5.15	78 (93%)
		1.0	0.006917	2.70	1.89	4.72	54 (7%)
				3.56		5.43	82 (93%)
	ZnCl$_2$	0.5	0.006050	3.50	1.22	2.78	41 (18%)
				4.36		3.10	57 (79%)
				7.47		4.06	128 (3%)
		0.75	0.006101	3.17	1.47	3.53	47 (13%)
				4.03		3.98	67 (85%)
				6.37		5.00	135 (2%)
		1.0	0.006831	3.09	1.63	4.04	52 (14%)
				3.85		4.51	73 (86%)

Numbers in brackets indicate the percentage of each fraction and are given considering 100% of the sum of the indicated main types of sedimenting species.

and of opposite sign. Nonetheless, a good fit for the two-binding-site model was generated. The obtained results showed that ggNucb2 preferentially formed monomer species and bound two Zn^{2+} ions, as the incompetent fraction stayed at 0. The first binding event occurred with a formation constant of approximately 190 μM and a binding enthalpy of −10 kcal/mol. The second binding event occurred with a much higher affinity of approximately 35 μM but with a small endothermic enthalpy of approximately +1 kcal/mol (Table 3). The corresponding entropic factor for the second event was very high compared with the entropic factor of the first binding with a +12 kcal/mol difference in $T\Delta\Delta S_{2-1}$. This result may suggest that the second process might be strongly influenced by the oligomeric state of the complex. Such conditions, however, effectively make fitted parameters questionable and uncertain.

Zn^{2+} binding to hsNucb2 (Fig. 6A) is represented by an exothermic process with threefold higher negative heats (in absolute values) than Zn^{2+}-titrated ggNucb2. Additionally, the hsNucb2 titration is represented by a monophasic isotherm with a single inflection point and a higher slope compared with the analogous titration of ggNucb2. The results were best fitted to the two-binding-site model with binding enthalpies of approximately −11 kcal/mol and −8 kcal/mol, respectively (Table 4). The calculated ΔG_{ITC} values were similar for both binding events, which seemed to be the consequence of the varied entropic contribution,

with the second site having a greater entropic impact than the other. These results suggested that the two binding sites may be differentiated in terms of ligands and may therefore be structurally and functionally different. An incompetent fraction of hsNucb2 was best fitted to approximately 0.5, suggesting that the protein in its apo form is predominately in a dimeric conformation (see Table 4).

Next, we focused on the thermodynamics of Mg^{2+} binding to both Nucb2s. Mg^{2+} titration of Nucb2s showed that one Mg^{2+} ion bound to one Nucb2 protein molecule (Fig. 5B and Fig. 6B) with a relatively high affinity (considering the millimolar buffering capacity of cells towards Mg^{2+} [60]) of approximately 200 μM, and the process was entropy-driven. Importantly, the presented heats were extremely small, increasing the uncertainty of the fitted parameters, especially ggNucb2. Mg^{2+} binding to ggNucb2 seemed to be an endothermic reaction; however, its heat rate was comparable to the dilution heat rate with a positive heat value, which almost entirely suppressed the resulting heat. Nevertheless, the presented results showed that both proteins differed significantly in terms of their qualitative assessment of Mg^{2+} binding, suggesting that the metal binding sites of both orthologues were not similar.

A previous study (see Ref. 49) revealed that both Nucb2s underwent Ca^{2+}-dependent structural modulation. HDX-MS showed that Ca^{2+} induced the compaction of two EF-hands of Nucb2s [49]. We
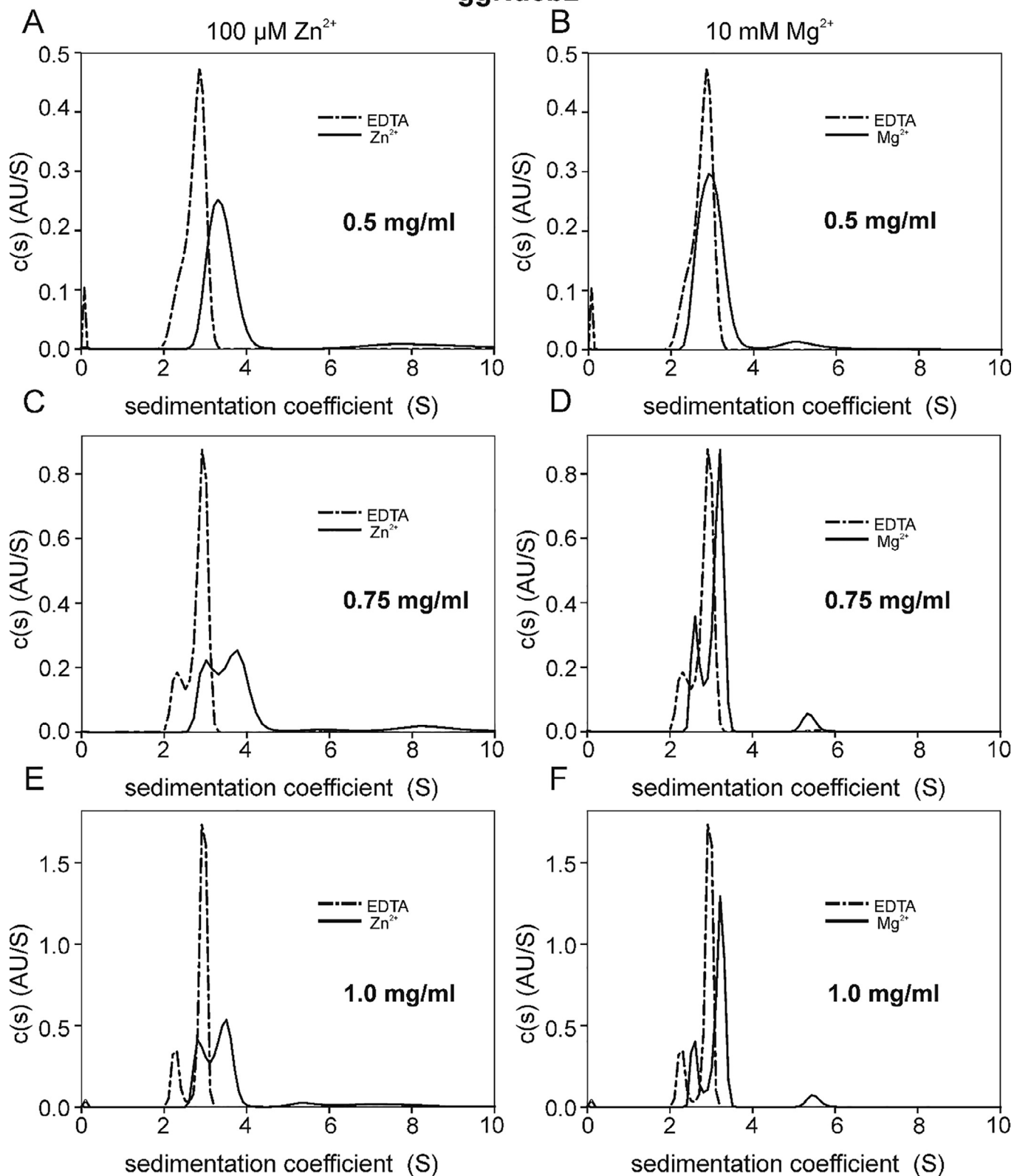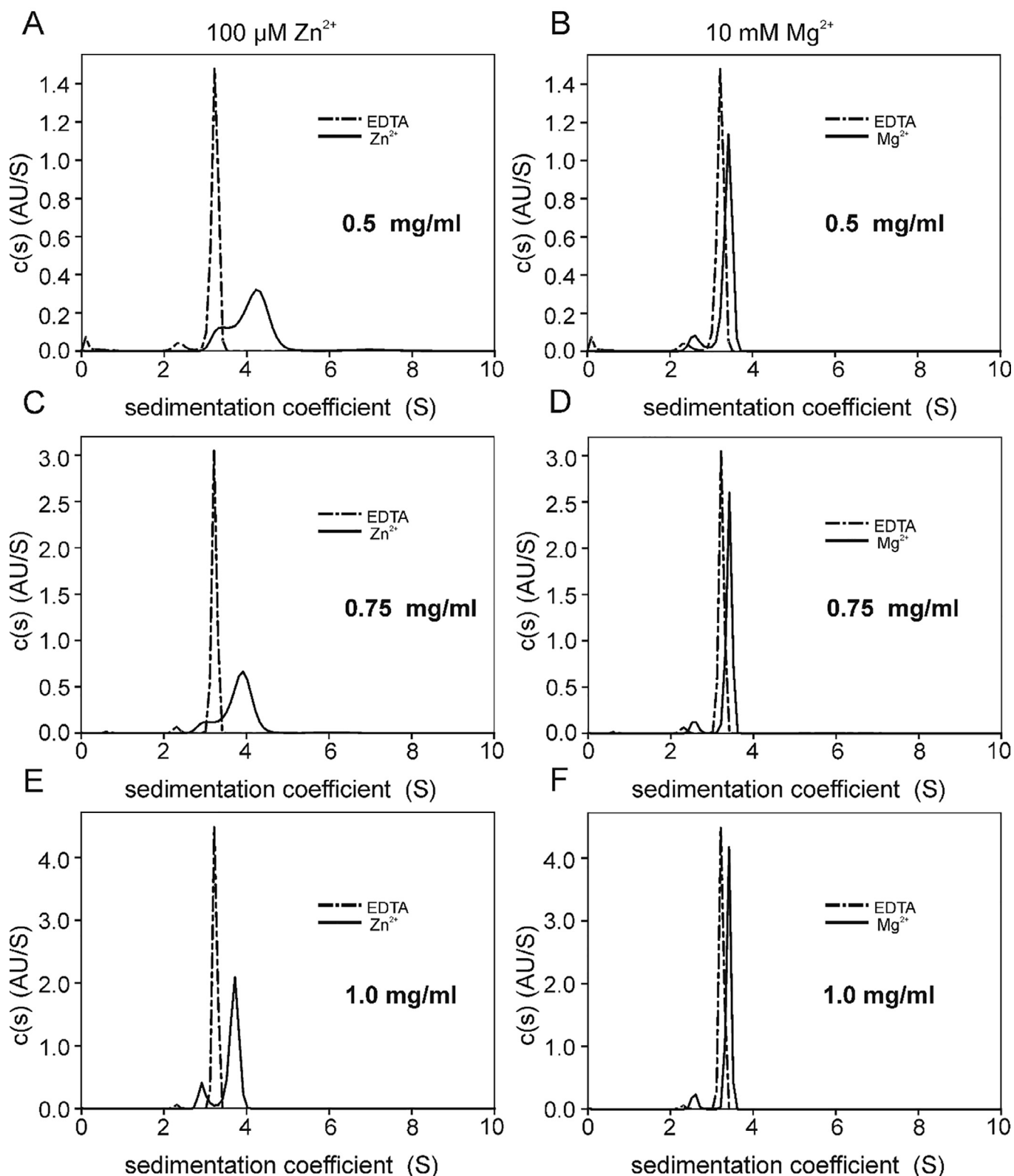
ggNucb2

Fig. 3. Size distribution characterization of ggNucb2 in the absence and presence of Zn^{2+} and Mg^{2+}. The SV-AUC measurements were performed for three concentrations of ggNucb2: 0.5 (A, B), 0.75 (C, D) and 1.0 mg/ml (E, F) in the presence of 5 mM EDTA, 10 mM Mg^{2+} and 100 μM Zn^{2+}, at 50 000 rpm and at 20 °C. Dash-dotted line – EDTA, solid line – appropriate metal ion.

also utilized ITC to determine the thermodynamic parameters of the Ca^{2+}-Nucb2s interaction. Ca^{2+} binding to ggNucb2 is represented by a biphasic process with increasing exothermic heats at

the beginning of titration (Fig. 5C). The exothermic process is described by the two-binding-site model, with substantially different affinities being observed for both sites. K_{d2} is approximately 5

hsNucb2

Fig. 4. Size distribution characterization of hsNucb2 in the absence and presence of Zn^{2+} and Mg^{2+}. The SV-AUC measurements were performed for three concentrations of hsNucb2: 0.5 (A, B), 0.75 (C, D) and 1.0 mg/ml (E, F) in the presence of 5 mM EDTA, 10 mM Mg^{2+} and 100 μM Zn^{2+}, at 50 000 rpm and at 20 °C. Dash-dotted line – EDTA, solid line – appropriate metal ion.

times lower than K_{d1}. Moreover, the first binding event was determined to be more entropy-driven, with the second being more enthalpy-driven (Table 3). Moreover, the incompetent protein frac-

tion was negligible, which suggests that ggNucb2 in its apo form is predominantly monomeric. Nonetheless, gradual increases in the exothermic process, clearly distinguishable for ggNucb2 titrated
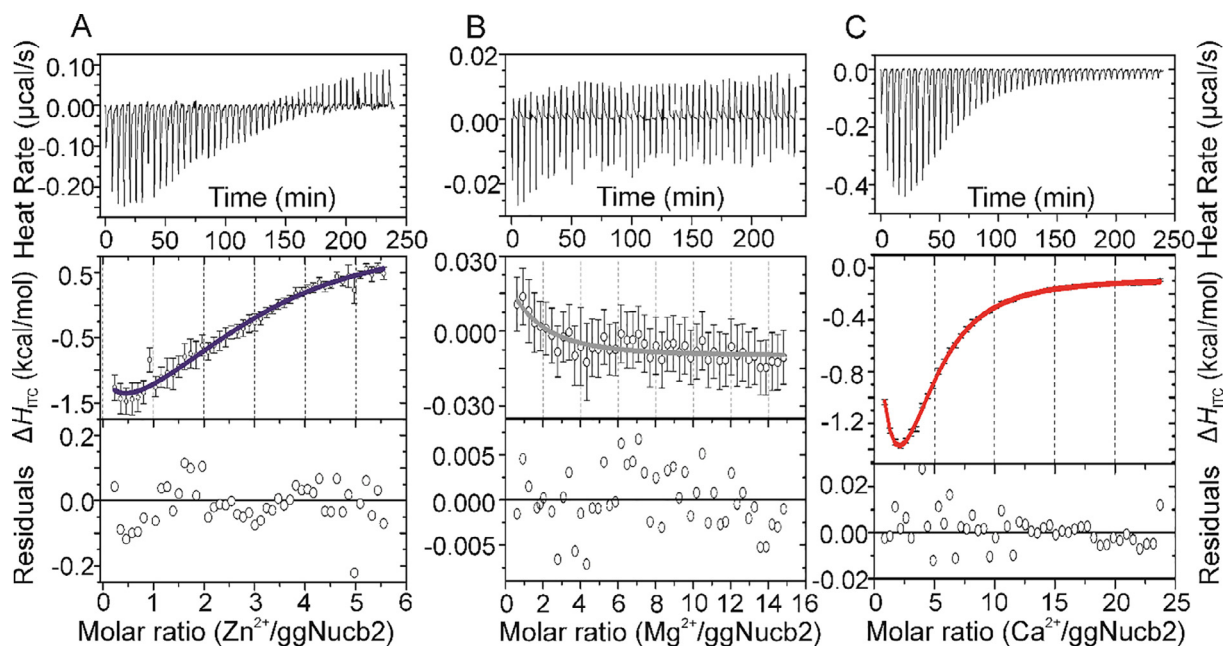
Fig. 5. ITC analysis of $Mg^{2+}/Zn^{2+}/Ca^{2+}$ binding to ggNucb2. (A) ITC profiles for Zn^{2+} binding to ggNucb2, (B) ITC profiles for Mg^{2+} binding to ggNucb2, (C) ITC profiles for Ca^{2+} binding to ggNucb2. The top panels show the baseline-subtracted thermograms. The bottom panels represent the binding isotherm. All measurements were obtained in 20 mM HEPES and 150 mM NaCl (pH 7.5).

Table 3
Thermodynamic parameters of Ca^{2+}, Mg^{2+} and Zn^{2+} complexation with ggNucb2 derived from fitting data to the ABB model of interactions with two symmetrical binding sites and parameters of Mg^{2+} complexation derived from fitting to the AB model (see Materials and methods).

Parameter	ggNucb2 + Zn^{2+}	ggNucb2 + Mg^{2+}	ggNucb2 + Ca^{2+} (narrow range)	ggNucb2 + Ca^{2+} (broad range)
[Nucb2] (µM)	46.2	104.8	50	50
[M^{2+}] (µM)	1000	6000	4000	4000
χ^2	1.05	0.33	1.9	2.8
K_{d1} (µM)	188 ± 3	230 ± 32	190.02 ± 0.79	302.8 ± 0.9
ΔH_1 (kcal/mol)	−10 ± 1	0.09 ± 0.11	−1.3 ± 0.2	−1.7 ± 0.1
$T\Delta S_1$ (kcal/mol)	−4.92	5.05	3.78	3.11
K_{d2} (µM)	34.38 ± 1.87	–	73.2 ± 0.7	60.6 ± 0.4
ΔH_2 (kcal/mol)	1.16 ± 0.48	–	−8.1 ± 0.3	−9.6 ± 0.8
$T\Delta S_2$ (kcal/mol)	7.25	–	−2.46	−3.85
Inc. Nucb2 fraction	0	0	0.00 ± 0.05	0.00 ± 0.10

Nucb2 – nucleobindin 2; M^{2+} – metal ion (Ca^{2+}, Zn^{2+} or Mg^{2+}); χ^2 – chi square, $K_{d1/d2}$ – dissociation constant for the first or the second binding site; $\Delta H_{1/2}$ – enthalpy of the complex formation for the first or the second binding site; $T\Delta S_{1/2}$ – entropic contribution for the first or the second binding event; Inc. Nucb2 fraction – incompetent protein fraction.

with Ca^{2+}, may be caused by the ligand-mediated association of protein monomers into dimers or higher oligomeric forms. Fitting accounting for this process suggested that metal ions shift the equilibrium of oligomerization towards dimers and that the process is cooperative. However, on the basis of the presented results alone, we cannot determine the values of the binding constants and cooperativity index values with certainty, as additional experimental conditions are necessary to obtain these parameters with precision (Table S1).

The binding of Ca^{2+} to the hsNucb2 protein (Fig. 6C) is very different from the binding of Ca^{2+} to ggNucb2. The binding process is represented by a monophasic isotherm, with the experimental heats being considerably more pronounced. In this analysis, the exothermic process was best fitted to the ABB model accounting for two symmetrical sites with a binding enthalpy for both sites of approximately −10 kcal/mol. The results show that two Ca^{2+} ions bind macroscopically identical to both sites of hsNucb2, contrary to ggNucb2. However, the fitted parameter of the incompetent protein fraction of approximately 0.5 suggested that 50% of protein molecules were not involved in the binding processes as

individuals, indicating that Ca^{2+} ions are bound by a dimeric unit of hsNucb2 (Table 4).

Nucb2s are in monomer-dimer equilibrium or even monomer-oligomer equilibrium in the case of the ggNucb2 homologue. This property makes the analysis of ITC isotherms challenging, as metal ion titration would be initiated into unstable oligomeric species. The clear differences in isotherm shapes of Zn^{2+} and Ca^{2+} binding to Nucb2s, as well as varied entropic factors, suggest that hsNucb2 is preferentially dimeric in the apo state, which stands in contrast to ggNucb2, which presents a significant fraction of monomer before metal ion addition, which is in keeping with the SV-AUC results.

2.5. Enhanced dynamics of Nucb2s showed by HDX-MS

Fluorescence spectroscopy showed that the structure of both Nucb2s undergoes compaction in the presence of Zn^{2+}. The AUC results revealed that Nucb2s have a compact shape and exist as oligomeric species in the presence of Zn^{2+}. The ITC measurements confirmed that Nucb2s are Mg^{2+}/Zn^{2+}-binding proteins. To investi-
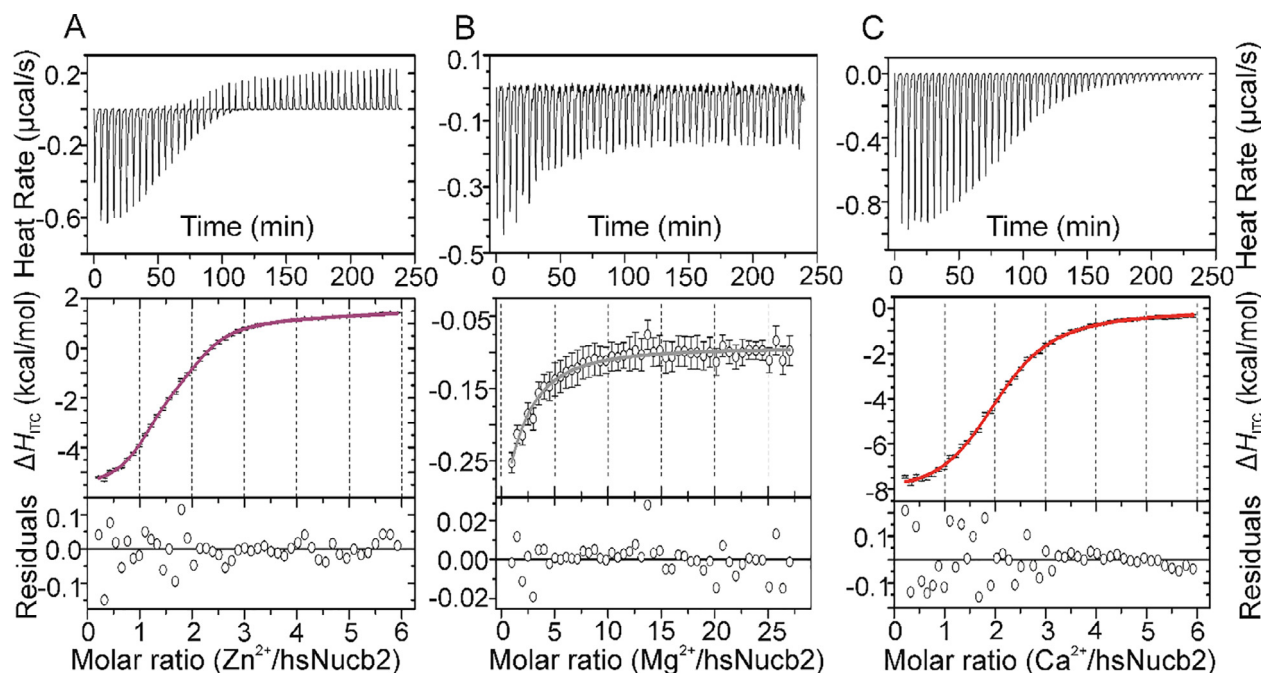
Fig. 6. ITC analysis of $Mg^{2+}/Zn^{2+}/Ca^{2+}$ binding to hsNucb2. (A) ITC profiles for Zn^{2+} binding to hsNucb2, (B) ITC profiles for Mg^{2+} binding to hsNucb2, (C) ITC profiles for Ca^{2+} binding to hsNucb2. The top panels show the baseline-subtracted thermograms. The bottom panels represent the binding isotherm. All measurements were obtained in 20 mM HEPES and 150 mM NaCl (pH 7.5).

Table 4
Thermodynamic parameters of Ca^{2+} and Zn^{2+} complexation with hsNucb2 derived from fitting data to the ABB model of interactions with two symmetrical binding sites and parameters of Mg^{2+} complexation derived from fitting to the AB model (see Materials and methods).

Parameter	hsNucb2 + Zn^{2+}	hsNucb2 + Mg^{2+}	hsNucb2 + Ca^{2+}
[Nucb2] (μM)	75.2	65.9	75.2
[M^{2+}] (μM)	1500	6000	1500
χ^2	0.42	0.71	4.8
K_{d1} (μM)	23.9 ± 0.2	203.21 ± 0.01	16.8 ± 0.2
ΔH_1 (kcal/mol)	−11.0 ± 0.3	−0.85 ± 0.02	−9.1 ± 0.2
$T\Delta S_1$ (kcal/mol)	−6.04	4.186	−2.61
K_{d2} (μM)	14.3 ± 0.7	–	19.8 ± 0.2
ΔH_2 (kcal/mol)	−8.4 ± 0.6	–	−10.4 ± 0.3
$T\Delta S_2$ (kcal/mol)	−1.76	–	−3.98
Inc. Nucb2 fraction	0.57 ± 0.01	0.00 ± 0.01	0.48 ± 0.07

Nucb2 – nucleobindin 2; M^{2+} – metal ion (Ca^{2+}, Zn^{2+} or Mg^{2+}); χ^2 – chi square, $K_{d1/d2}$ – dissociation constant for the first or the second binding site; $\Delta H_{1/2}$ – enthalpy of the complex formation for the first or the second binding site; $T\Delta S_{1/2}$ – entropic contribution for the first or the second binding event; Inc. Nucb2 fraction – incompetent protein fraction.

gate the impact of Zn^{2+} and Mg^{2+} binding on the structure and conformational dynamics of Nucb2s and to identify the potential residues or regions involved in these binding events, we utilized HDX-MS. The HDX-MS technique is based on the monitoring of the exchange of amide hydrogen to deuterium. The rate of these exchanges depends on the conformational flexibility of the protein's backbone, solvent accessibility, and hydrogen bonding status [61,62]. Amide hydrogens involved in bonding and located within the secondary and tertiary structural elements exchange slowly. In contrast, the exchange of amide hydrogens exposed to the solvent and not engaged in ordered structural elements is rapid [63,64]. HDX-MS is currently used to detect IDRs in proteins due to its ability to differentiate between protein regions of diverse deuterium exchange protection [65].

Before each experiment, both proteins were digested using an immobilized Nepenthesin-2 column to produce a peptide map

enabling the best coverage of the protein sequence. For HDX-MS analysis, 161 peptides of ggNucb2 covering 92.4% of the sequence and 200 peptides of hsNucb2 covering 95.0% of the sequence were selected. We followed the hydrogen to deuterium exchange of Nucb2s over a time course of 10 s to 1 h. The structure of Nucb2s (Fig. 7A and Fig. 8A) was first studied to obtain wide structural information on ligand-free protein molecules. The C-terminal halves of both proteins were characterized by fast HDX (Fig. 7A and Fig. 8A), suggesting that they have high conformational flexibility and are structurally dynamic. In contrast, the N-terminal halves of Nucb2s were characterized by a mosaic-like structure consisting of regions with rapid or slow HDX rates. Notably, the level of deuterium uptake observed for peptides encompassing amino acid residues 33–45, 80–97 and 135–140 in the ggNucb2 sequence (Fig. 7B) did not reach the maximal value even after 1 h. Such structural protection indicates that these regions form a very stable core structure. The results obtained in this analysis were in keeping with previously presented findings for both His-tagged apo-Nucb2 proteins (see Ref. 49).

To characterize the Zn^{2+}-induced conformational rearrangements of Nucb2s, we examined the HDX rate in the presence of these metal ions. In the presence of 100 μM Zn^{2+} (Fig. 7C and Fig. 8C), changes in deuterium uptake only occurred at the N-terminal half of the Nucb2s. Three regions (peptides 32–55, 72–94 and 115–149) of ggNucb2 (Fig. 7C and D) and three regions of hsNucb2 (peptides 33–55, 71–94 and 129–138) (Fig. 8C and D) had higher deuterium uptake after the addition of Zn^{2+}, indicating the increased solvent accessibility of these regions. Notably, a change in the HDX level of Nucb2s occurred in the region of the putative Zn^{2+}-binding site HFREX$_n$H [48]. For hsNucb2, the major HDX differences between apo- and Zn^{2+}-hsNucb2 were prominent at early time points: 10 s and 1 min (data not shown). After 10 min of exchange, the difference was not detected (data not shown). The increase in solvent exposure within 10 s was higher in holo-hsNucb2 than that observed for Zn^{2+}-ggNucb2. However, differences in the conformational flexibility and solvent exposure between Zn^{2+}- and EDTA-ggNucb2 were still observed for peptides
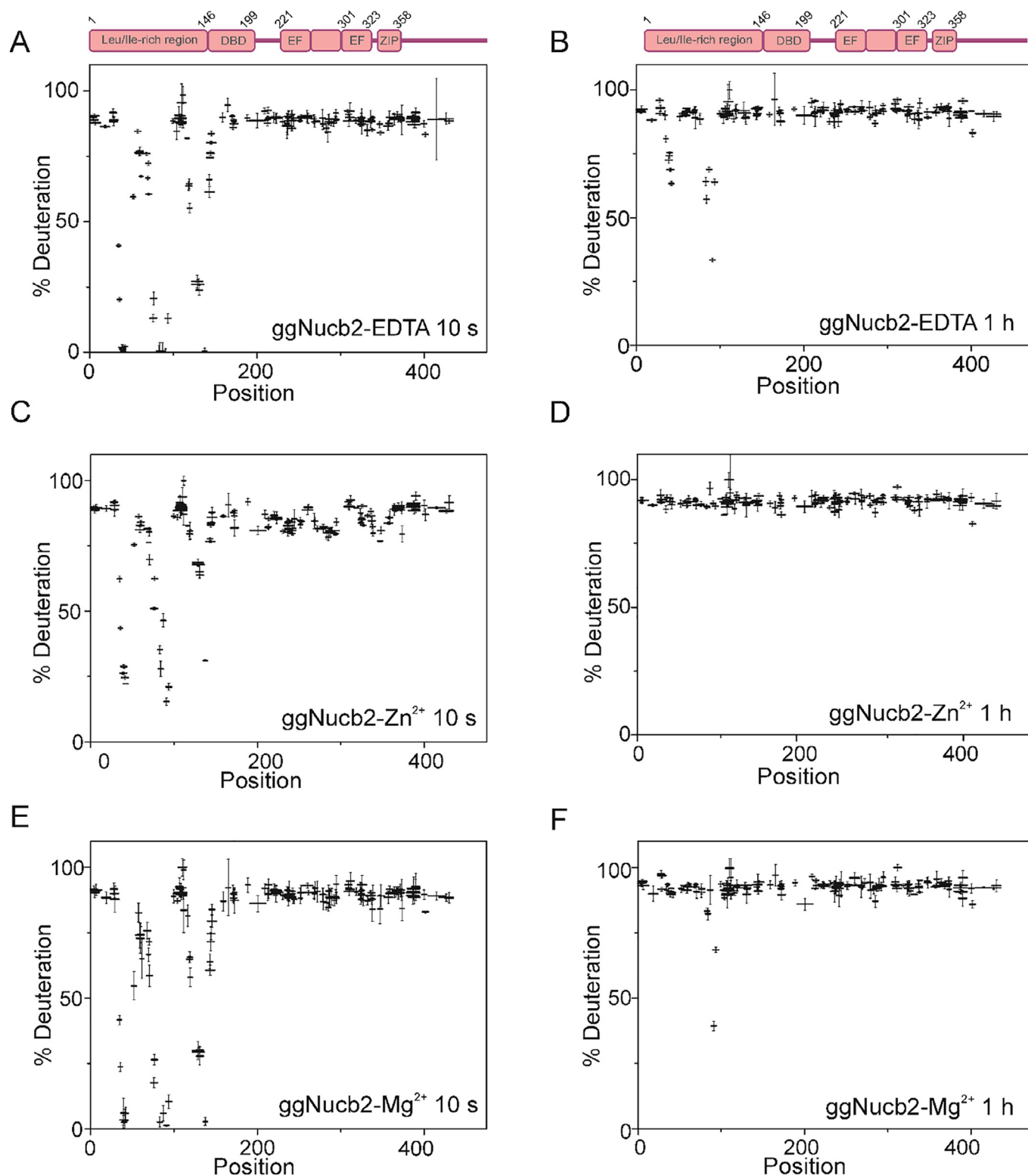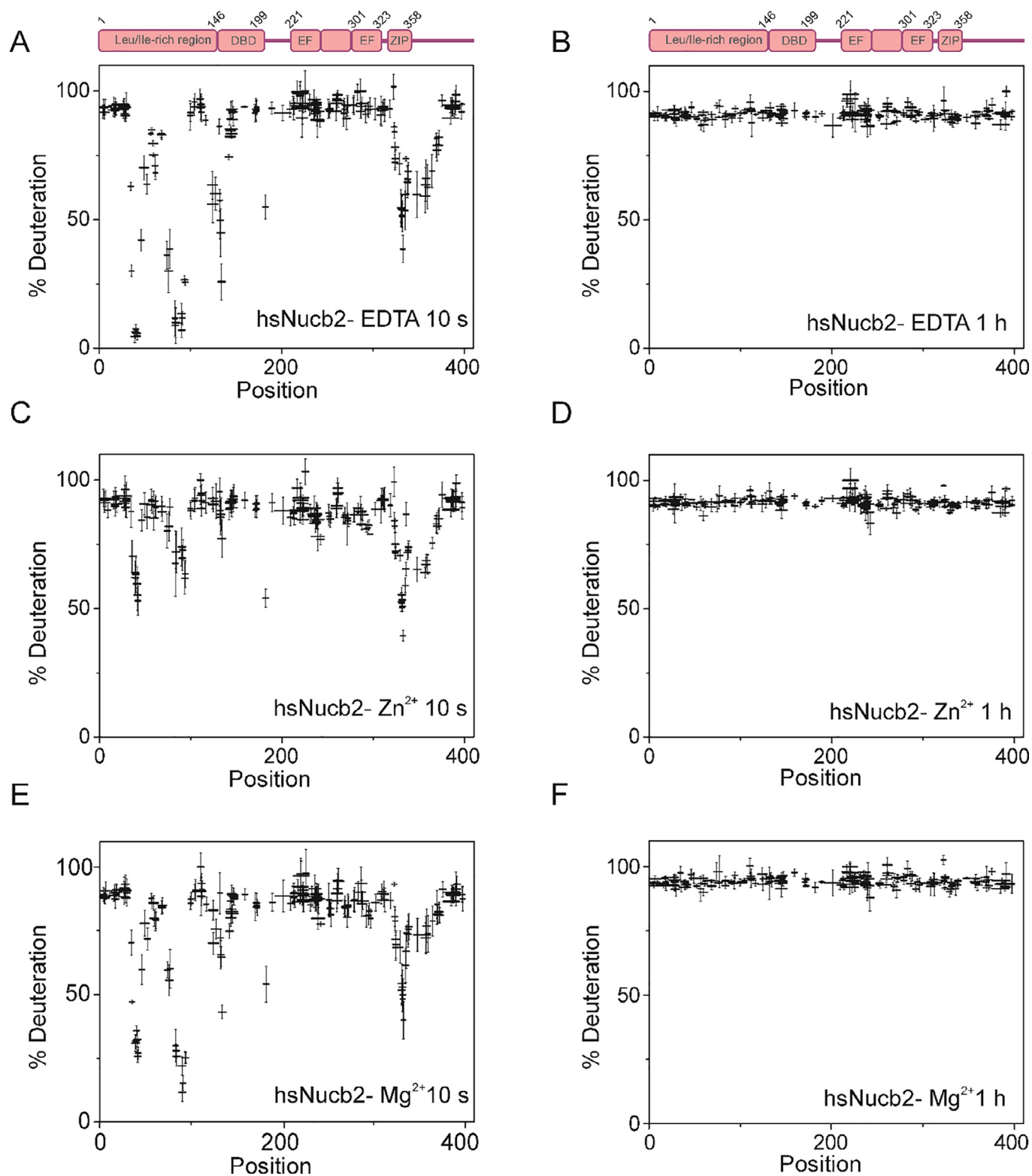
Fig. 7. Percentage of deuteration in peptides from ggNucb2 in the absence and presence of 100 μM Zn^{2+} and 10 mM Mg^{2+}. The graphs represent HDX patterns after 10 s (A, C, E) and 1 h (B, D, F) incubation with D_2O. The error bars represent the standard deviations of three independent experiments.

33–45, 80–97 and 135–140 even after a one-hour exchange (Fig. 7B and D).

Next, we investigated the effect of Mg^{2+} on the solvent accessibility of Nucb2 proteins. The HDX-MS experiment in the presence of 10 mM Mg^{2+} was performed under the same conditions as in the presence of 5 mM EDTA and 100 μM Zn^{2+}. The HDX pattern of

ggNucb2 in the presence of EDTA and Mg^{2+} was notably similar (Fig. 7E and F), which was in keeping with the CD and fluorescence spectra results. However, the ITC revealed that ggNucb2 bound one Mg^{2+}. This result indicated that the binding of Mg^{2+} by ggNucb2 might not induce significant structural rearrangements of the protein structure. Notably, the deuterium uptake level of hsNucb2

Fig. 8. Percentage of deuteration in peptides from hsNucb2 in the absence and presence of 100 µM Zn^{2+} and 10 mM Mg^{2+}. The graphs represent HDX patterns after 10 s (A, C, E) and 1 h (B, D, F) incubation with D_2O. The error bars represent the standard deviations of three independent experiments.

(Fig. 8E and F) was slightly increased in the presence of Mg^{2+}. Changes in deuterium incorporation were visible in the N-terminal half of hsNucb2 (peptides 33–49, 71–94 and 129–138), which was also observed for Zn^{2+}. However, the increase in deuterium incorporation in the presence of Mg^{2+} was less pronounced. Overall, the presence of Zn^{2+} ions led to increased solvent exposure of the N-terminal half of the Nucb2s, which was probably due to destabilization of this protein part. Furthermore, Zn^{2+}-dependent structural changes were more significant for ggNucb2. The presence of Mg^{2+} was only determined to have an impact on the solvent accessibility of hsNucb2. Similar to Zn^{2+}, the addition of Mg^{2+} led to increased flexibility of the N-terminal part of hsNucb2. However,

the change in the HDX level in the presence of Mg^{2+} was smaller than that in the presence of Zn^{2+}.

2.6. Change in the structural parameters of Nucb2 characterized by SAXS

Trp fluorescence spectra analysis and AUC data showed that in the presence of Zn^{2+}, Nucb2s undergo compaction and oligomerization. Moreover, HDX-MS revealed solvent exposure at the N-terminal half of the Nucb2s. To further investigate the structural changes of Nucb2s induced by metal ions, we employed SAXS, which is a powerful biophysical technique that provides information regarding the overall shape and size of molecules in solution under various conditions [66,67]. This method is frequently used to study different IDPs [68]. We performed SAXS analyses of both Nucb2s in the absence and presence of Zn^{2+}, Mg^{2+} and Ca^{2+}. The scattering data of both Nucb2s in the absence and presence of metal ions were qualitatively assessed by means of a Kratky plot (Fig. 9A and B). All SAXS curves of Nucb2s showed a broad, asymmetric peak and a plateau followed by a further decrease at large S values. This behaviour is characteristic of partially disordered proteins and multidomain proteins [69].

The radius of gyration, R_g, which is determined from the Guinier plot's slope, is frequently used to quantify the average size of macromolecules [70]. The R_g is higher for partly extended or even fully disordered proteins than for globular particles [71]. The R_g values for ggNucb2 and hsNucb2 in the presence of EDTA were calculated to be 66.5 ± 1.9 Å and 67.6 ± 2.3 Å, respectively (Table 5). Notably, in the presence of metal ions (Zn^{2+}, Mg^{2+} and Ca^{2+}), the R_g

for both Nucb2s decreased, suggesting the compaction of the Nucb2 molecules. The change in R_g was observed to be most significant for Zn^{2+}-Nucb2s. The pair distance distribution function, $p(r)$ (which is a histogram of all the distances within the protein molecule [68]), was calculated for all the apo- and holo-forms of Nucb2 by indirect Fourier transform of the scattering intensity using the GNOM program [72]. The $p(r)$ functions for all forms of Nucb2 were determined to be asymmetric and displayed extended tails (see examples in Fig. 9C and D), which is typical for proteins with an elongated shape. This property was also indicated by the large maximum particle dimension (D_{max}) values of all the Nucb2 forms. However, in the presence of analysed metal cations, the D_{max} values decreased for both Nucb2. The only exception was observed for Zn^{2+}-ggNucb2, where binding of Zn^{2+} led to an increase in the D_{max} value (Table 5). Notably, the characteristic shape of the Nucb2s' $p(r)$ function indicated the presence of two species in solution. Therefore, we also applied the obtained experimental SAXS data to determine the molecular mass and the oligomeric state of both proteins. The method uses the extrapolated intensity I(0) on a relative scale, and its further comparison with I(0) from a standard protein with known molecular mass (here BSA) was chosen for this purpose. The analysis revealed that ggNucb2 in apo- and all holo-forms, as well as hsNucb2 in the presence of Zn^{2+}, existed in the solution as a mixture of monomers and dimers, while the dominant form of apo- and Mg^{2+}/Ca^{2+}-hsNucb2 in solution was a dimer. These results were in keeping with the presented AUC data. The differences in $p(r)$ shape through the different forms of both Nucb2s may be attributable to structural reorganization within the molecular species.
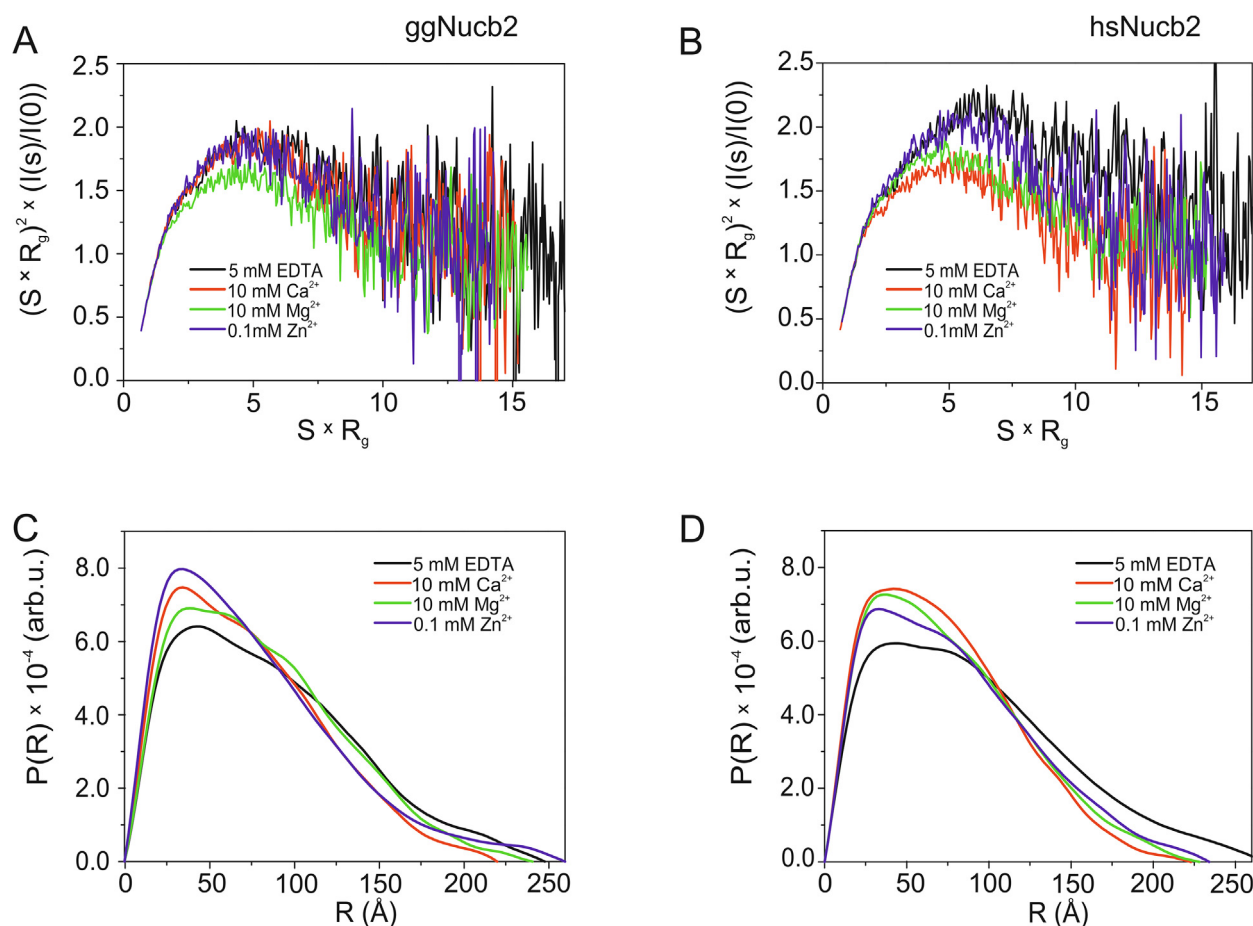

Fig. 9. SAXS analysis of Nucb2s. Dimensionless Kratky plot of ggNucb2 (A) and hsNucb2 (B). The pair distribution function $p(r)$ of ggNucb2 (C) and hsNucb2 (D). SAXS measurements were carried out on Nucb2 in the presence of 5 mM EDTA, 10 mM Ca^{2+}, 10 mM Mg^{2+} and 100 μM Zn^{2+}.

Table 5
Structural parameters of Nucb2s in the absence and presence of different metal ions determined from SAXS data.

Agent	R_g [Å]	D_{max} [Å]	MM [kDa]
ggNucb2			
5 mM EDTA	66.5 ± 1.9	248	82.75
10 mM Mg^{2+}	60.5 ± 1.6	240	85.91
100 μM Zn^{2+}	55.29 ± 1.68	260	67.68
10 mM Ca^{2+}	58.85 ± 1.19	220	75.39
hsNucb2			
5 mM EDTA	67.62 ± 2.27	268	91.87
10 mM Mg^{2+}	58.92 ± 1.76	228	92.92
100 μM Zn^{2+}	61.64 ± 1.40	234	82.40
10 mM Ca^{2+}	55.73 ± 1.13	223	93.62

2.7. Metal-ion-dependent morphology of Nucb2 aggregates

During CD and ITC experiments, we observed that ggNucb2 underwent precipitation upon a higher concentration of Zn^{2+}. Additionally, the AUC showed that Nucb2s in the presence of Zn^{2+} existed in the solution as high-molecular-weight assemblies and that precipitation of ggNucb2 was induced by a Zn^{2+} concentration of ≥300 μM. To visualize the morphology of higher-molecular-weight aggregates of ggNucb2, we monitored the supernatant and insoluble precipitate of 0.5 mg/ml ggNucb2 obtained after AUC by transmission electron microscopy (TEM). TEM images revealed that ggNucb2 precipitates were spherical aggregates and irregular assemblies of amorphous aggregates (see Fig. S3), distributed evenly. On the other hand, ggNucb2 isolated from the supernatant fraction consisted of spherical aggregates with an average diameter of 24 ± 4 nm and elongated particles with an average diameter of 32 ± 14 nm (Fig. S3).

To further analyse the morphology of Nucb2 aggregates, TEM images were obtained at different time points (0–2 weeks) for Nucb2s incubated in the absence and presence of 300 μM Zn^{2+}, 10 mM Mg^{2+} and 10 mM Ca^{2+}. We chose 300 μM Zn^{2+} as a critical concentration, which induced the greatest oligomerization changes revealed by SV-AUC and led to protein precipitation when the protein concentration was maintained at or below 0.5 mg/ml. In the absence of metal ions, both Nucb2s formed spherical aggregates that were similar in size even after a 2-week incubation period (Fig. 10A and B). The heterogeneous mixture of Nucb2 round particles was observed at 10 mM Ca^{2+}. Notably, the size of Nucb2 aggregates in the presence of Ca^{2+} decreased over time. A similar tendency was seen for Mg^{2+}-hsNucb2 particles. In contrast, the size of ggNucb2 spherical aggregates in the presence of Mg^{2+} increased throughout the two-week incubation period. However, the most significant alterations in the morphology of Nucb2 aggregates were observed in the presence of Zn^{2+}. The incubation of ggNucb2 with 300 μM Zn^{2+} resulted in spherical aggregates and elongated particles (Fig. 10A), even after two weeks. In contrast, in the presence of Zn^{2+}, hsNucb2 formed well-dispersed aggregates (see Fig. 10B). These results were consistent with the previously described AUC data. Zn^{2+} bound to Nucb2s, inducing the formation of higher-order aggregates. This effect was more visible for ggNucb2.

3. Discussion

The binding of metal ions impacts the structure of proteins which, in turn, may be engaged in the regulation of their functions [73,74]. Metal ion binding might lead to disorder-to-order transition [75], destabilization of the structure [76], oligomerization [77] and even aggregation [78] of the protein. Changes in the protein structure in the presence of various metal ions might facilitate the adaptation to specific protein functions. Among all metal ions,
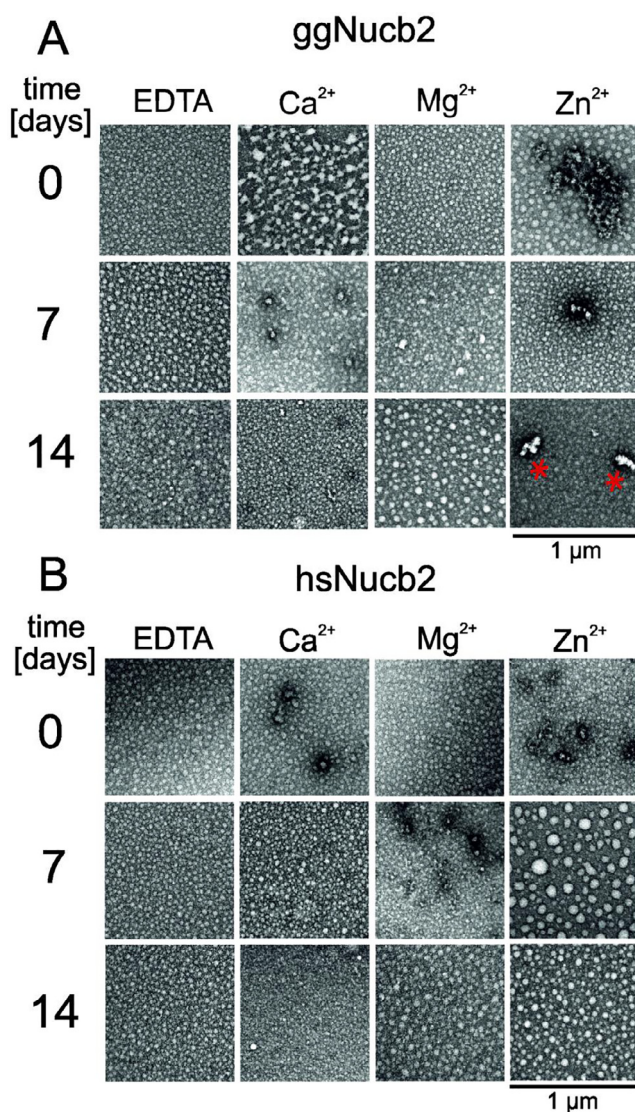

Fig. 10. Transmission electron microscopy (TEM) micrographs of Nucb2 aggregate morphology in the presence of divalent metal ions at different time points. (A) Representative TEM images of ggNucb2 aggregates generated in the absence and presence of 10 mM Ca^{2+}, 10 mM Mg^{2+} and 300 μM Zn^{2+} in the 0–14-day periods. (B) Representative TEM images of hsNucb2 aggregates generated in the absence or in the presence of 10 mM Ca^{2+}, 10 mM Mg^{2+} and 300 μM Zn^{2+} in the 0–14-day periods. The red asterisks indicate the elongated particles. Scale bars represent 1 μm. (For interpretation of the references to colour in this figure legend, the reader is referred to the web version of this article.)

Ca^{2+}, Zn^{2+}, and Mg^{2+} are the most relevant for modulating protein function [79]. Previous research [49] revealed that Ca^{2+} has a strong impact on the structure of Nucb2s. The interaction between Ca^{2+} and Nucb2s resulted in a disorder-to-order transition and dimerization of both proteins [49]. In the structure of Nucb2s, two EF-hand domains are present, which are responsible for Ca^{2+}/Mg^{2+} binding [6] and one putative motif of Zn^{2+}-binding [48]. In this study, we determined the thermodynamic properties of Nucb2s interacting with Mg^{2+} and Zn^{2+}, as well as their influence on the structure of Nucb2s. The far-UV CD indicated that Zn^{2+} slightly modulated the secondary structure of Nucb2s. HDX-MS analysis revealed that upon the addition of Zn^{2+}, the solvent accessibility of regions of the N-terminal half (containing nesfatin-1 and -2) of Nucb2s is changed (increased), leading to a decrease in the stability of the protein molecule. The structural dynamics change of ggNucb2s in the presence of Zn^{2+} was found to be even more

pronounced. On the other hand, Trp emission spectra showed that Nucb2s upon Zn^{2+} binding undergo structural compaction, which is in keeping with limited proteolysis (see Figs. S5 and S6), SV-AUC study and SAXS data. Both of the Trp residues of Nucb2s are located at the C-terminal half, i.e., nesfatin-3. These results suggest that Zn^{2+} might also affect the structure of nesfatin-3. Therefore, we conclude that for both homologues, Zn^{2+} binding manifests itself by significant conformational changes, which seem to also be consequences of changes in the secondary structure of both protein molecules. In contrast, Mg^{2+} binding does not seem to be followed by ggNucb2 secondary structure alternation according to CD and fluorescence data, indicating a different binding mechanism for this ligand. Mg^{2+} induces, however, a slight increase of α-helical content of hsNucb2. We also did not observe compaction of Mg^{2+}-saturated ggNucb2 with only a minor compaction of the Mg^{2+}-hsNucb2 molecule. Mg^{2+} binding may, however, change the monomer-oligomer equilibrium, especially for ggNucb2. Additionally, HDX-MS showed that the presence of Mg^{2+} slightly affects conformational flexibility but only affects hsNucb2. Notably, both Zn^{2+}/Mg^{2+} ions affect the oligomeric state of Nucb2s. Apo-ggNucb2 behaves as a monomer in the solution. ggNucb2 in the presence of Mg^{2+} consists of monomeric species and a low amount of dimeric species. These results suggest that the addition of Mg^{2+} changes the equilibrium between the monomeric and dimeric forms of ggNucb2, leading to dimeric form stabilization. In contrast, hsNucb2, in its apo- and holo-(Mg^{2+}) form, exists primarily in a dimeric form. Surprisingly, Zn^{2+} addition results in the appearance of high-molecular-weight assemblies of Nucb2s, which are more evident for ggNucb2. TEM images revealed that the addition of Zn^{2+} resulted in the formation of characteristic aggregates that were well dispersed and elongated for hsNucb2 and ggNucb2, respectively. Additionally, a high concentration of Zn^{2+} ($\geq$300 µM) induces the precipitation of ggNucb2 during the CD, fluorescence and SV-AUC experiments. TEM analysis visualized the appearance of characteristic assemblies of amorphous aggregates in the ggNucb2 precipitate and elongated particles in the isolated supernatant form of ggNucb2. Notably, similar irregular assemblies were observed for the intermediate filament protein vimentin in the presence of Zn^{2+} [80]. These vimentin fibrils are not able to mediate filament formation [80]. Vimentin is expressed in mesenchymal cells and participates in such processes as cell division, migration and signalling [81–83]. Vimentin is also known as a marker and agent of the epithelial to mesenchymal transition (EMT) process [84,85]. Surprisingly, previous research suggested that Nucb2 is involved in EMT [41,86]. This Zn^{2+}-dependent structural alteration of Nucb2 molecules might be connected with the role of Nucb2 in the tumorigenesis process. However, the precipitation and formation of similar aggregates in the presence of elevated Zn^{2+} concentrations were also observed, e.g., neuronal calcium sensor-1 (NCS-1) protein [87] and insulin [88]. Brain cells [89] and β cells in the pancreas [24] are characterized by high levels of Zn^{2+}. Zn^{2+} participates in both brain physiology and pathology, and it is essential to maintain normal brain activity and proper protein function [90]. On the other hand, alterations in Zn^{2+} levels are implicated in central nervous system disorders, such as neurodegenerative diseases [91,92] and mental dysfunction, e.g., depression [28] and schizophrenia [93]. Moreover, Zn^{2+} ions are implicated in β-cell insulin formation, storage and secretion [94,95]. Notably, an elevated expression level of Nucb2 was found in the central nervous system, i.e., the hypothalamus and pituitary gland [38,96], and in pancreatic β cells [45]. Additionally, it was shown that Nucb2 and nesfatin-1 promote insulin secretion, which suggests the antidiabetic properties of these proteins [97]. The physiological importance of Zn^{2+} for Nucb2 function has not been determined. Taken together, our results suggest that Zn^{2+} binding to the Nucb2 molecule leads at first to the solvent exposure of peptides at the N-terminal half of Nucb2s, probably enabling structural changes at the C-terminal half of Nucb2s and the formation of oligomeric species of both homologues. These formed oligomers/aggregates might constitute physiological or pathological forms of Nucb2s. The question of whether this self-association and/or precipitation would be physiologically relevant merits further investigation.

To gain insights into the binding of Zn^{2+}/Mg^{2+} to Nucb2s, we used ITC. The Mg^{2+}-Nucb2 interaction for both homologues appeared to be highly similar. ITC demonstrated the existence of one binding site for Mg^{2+} with high affinity. On the other hand, the binding of Zn^{2+} by both Nucb2s was found to be more complex. Although Zn^{2+} binding events were predominately exothermic processes, thermograms involved a small fraction of endothermic heats. Moreover, the interaction of ggNucb2 with Zn^{2+} exhibited significantly more complicated behaviour than hsNucb2. At a lower concentration of Zn^{2+}, the exothermic reaction was determined to coincide with an endothermic process, as demonstrated by gradually increasing negative heats at the first several injection points. In contrast, at the higher Zn^{2+} concentration range, immediately before the exothermic reaction plateau, a substantial endothermic event was observed to arise. Based on our analysis, we strongly suggest that the first process is a direct cause of Zn^{2+}-induced dimerization of ggNucb2, and the second is due to the formation of higher-order oligomers or even precipitation that is typical for this protein under excess Zn^{2+}. In contrast, the hsNucb2-Zn^{2+} interaction is characterized by a threefold increased heat rate. The endothermic process caused by Zn^{2+}-dependent dimerization was not observed, indicating *a priori* dimerized protein in the apo form. Nonetheless, significant positive heats at the plateau of the titration isotherm were observed, as in the case of ggNucb2. Such endothermic processes might arise from Nucb2 oligomerization. It is commonly observed that in the presence of excess Zn^{2+}, a higher assembly of protein oligomers may be formed. Similar thermodynamic properties associated with oligomerization in the presence of Zn^{2+} were observed for insulin monomers [88], soybean ASR protein [78] and one of the late embryogenesis abundant proteins AtLEA4-5 [98]. Notably, the hsNucb2-Zn^{2+} interaction is different from that observed for hsNucb1. Nucb1, the paralogue of Nucb2, was previously characterized [48] as a Zn^{2+} sensor with a high affinity for Zn^{2+} with two Zn^{2+}-binding sites (K_d = 32 nM). In contrast, the fitted complex formation constants for both Zn^{2+}-binding sites of hsNucb2 are in the range of 10^{-5} M and seem to be significantly lower than those of Nucb1 [48], and hsNucb2 is characterized as a weak Zn^{2+}-binding protein, as Zn^{2+} is tightly buffered in the cell at concentrations in the low nanomolar to picomolar range [99]. Nucb2 amino acid sequences were determined to possess only one putative Zn^{2+} binding site, which might implicate these protein differences [48]. Taken together, all of the results discussed above suggest that the paralogues might fulfil different functions, despite the 62% amino acid sequence identity of hsNucb1 and hsNucb2 [100].

The N-terminal half of Nucb2 contains two out of three polypeptides derived from the precursor protein *in vivo*, i.e., nesfatin-1 and nesfatin-2. There is accumulating evidence regarding the pleiotropic function of nesfatin-1, which is involved in various processes, such as food intake inhibition [38], glucose homeostasis [45], cardiovascular functions [101], and stress behaviour [102]. The role of nesfatin-2 is unknown to date. Notably, a sequence-based analysis of Nucb2s performed with Aggrescan [103] and FoldAmyloid [104], web-based software for the prediction of aggregation-prone segments in protein sequences, identified the aggregation propensity regions within Nucb2s (Fig. S7). These regions were located primarily at the N-terminal half of both homologues. Further research is required to elucidate the full role of the N-terminal half of Nucb2 in this process and its implications.

The question remains whether nesfatin-1 and nesfatin-2, either separate from each other or as a part of a full-length precursor protein, might be involved in an aggregation process more efficiently. What is the role of Zn^{2+} binding? Can we link this aggregation propensity of Nucb2 with those exhibited by other amyloidogenic proteins? Notably, Nucb1, a paralogue of Nucb2, has been shown to be a chaperone-like amyloid binding protein [105–107]. Nucb1 binding stabilizes the protofibril intermediate of such proteins as IAPP, αβ, transthyretin, and α-synuclein [105–107]. Nucb1 prevents fibril formation at any stage of this process [105,107]. However, Ca^{2+} binding leads to disruption of the anti-amyloidogenic activity of Nucb1 [105,107], suggesting that both proteins might play similar roles. Nevertheless, our study indicated substantial differences between the mechanisms of action of these two paralogues.

We also analysed the thermodynamics of Ca^{2+} binding to Nucb2s. ITC revealed that both Nucb2s contain two Ca^{2+}-binding sites, which is in keeping with previously obtained HDX-MS results [49]. The Ca^{2+} binding process differs for both Nucb2s. The enthalpy of Ca^{2+} binding is considerably lower for ggNucb2, which might be caused by the varied oligomeric state of apo-Nucb2s. Previous SV-AUC data showed that ggNucb2 undergoes dimerization in the presence of Ca^{2+} [49]. However, hsNucb2 in the apo- and holo-(Ca^{2+}) states is dimeric [49].

In conclusion, our results showed that Nucb2s bind Zn^{2+} and Mg^{2+}, which affects the structure of Nucb2s. We surmise that the destabilization of the N-terminal half of Nucb2s enables intermolecular interactions, which promote the oligomerization/fibrilization of Nucb2s. Our previous and current research revealed that the structure of Nucb2s is divided into two parts: the Zn^{2+}-sensitive N-terminal half (consisting of nesfatin-1 and -2) and the Ca^{2+}-sensitive C-terminal half (consisting of nesfatin-3). Structural changes to Nucb2s in the presence of appropriate metal ions probably enable the protein to fulfil different physiological functions. However, further experiments are necessary to elucidate the molecular mechanisms underlying the metal ion-dependent functions of the Nucb2s.

4. Materials and methods

4.1. Chemicals

All buffers were prepared at room temperature. Buffer A contained 50 mM $Na_2HPO_4 \cdot 2\ H_2O$ and 300 mM NaCl (pH 7.0). Buffer B was 50 mM $Na_2HPO_4 \cdot 2\ H_2O$, 300 mM NaCl, and 200 mM imidazole (pH 7.0). Buffer C contained 20 mM Tris-HCl, 150 mM NaCl (pH 7.5). Buffer D contained 20 mM HEPES, 150 mM NaCl (pH 7.5). The quench buffer contained 2 M glycine (pH 2.53). DNase I and RNase A, $ZnCl_2 \cdot 2\ H_2O$, $MgCl_2 \cdot 6\ H_2O$, $CaCl_2 \cdot 2H_2O$ and EDTA were purchased from Sigma-Aldrich. All other chemicals were of analytical grade and commercially available.

4.2. Protein expression and purification

The ggNucb2 and hsNucb2 coding sequences were amplified by polymerase chain reaction (PCR) with One-Fusion DNA polymerase (Gene ON) and with primers introducing the SacI and HindIII restriction sites. The purified PCR products were digested with SacI and HindIII restriction enzymes and ligated into the pQE-80L/HRV3C vector, modified in our laboratory to introduce the HRV 3C protease cleavage sequence at the N-terminus of the target protein. This approach enabled further investigation of a tag-free protein with only four extra amino acid residues (Gly-Pro-Glu-Lys) added eventually at the N-terminus, which are derived from the HRV 3C protease cleavage sequence. The sequences in the DNA constructs were verified by Sanger sequencing (Genomed S.A.). Both Nucb2s were expressed and purified as reported previously [49]. Before the final size exclusion chromatography (SEC), proteins were digested with HRV 3C protease using a 100:1 (w/w) protein-to-protease ratio overnight at 4 °C and concentrated on Amicon Ultra-4 centrifugal filter units (Millipore). Proteins purified for ITC analyses were incubated with 5 mM EDTA for 1 h before SEC and eluted from the column with buffer D. The elution fractions were monitored by A_{280} measurements. The protein concentrations were measured at 280 nm utilizing the following extinction coefficients: ggNucb2 – 21,430 $M^{-1} \times cm^{-1}$ and hsNucb2 – 24,410 $M^{-1} \times cm^{-1}$, which were estimated from the amino acid sequence. The homogeneity and chemical identity of targeted proteins were evaluated by mass spectrometry and SDS-PAGE analyses.

4.3. Circular dichroism (CD)

Far-UV CD spectra were obtained using a JASCO J-815CD spectropolarimeter equipped with a Peltier-type temperature controller (Type Control System, JASCO) with a 1-mm path length quartz cuvette. The measurements were performed for both Nucb2s in buffer C in the absence (5 mM EDTA) and presence of 10 mM $MgCl_2$ or 100 μM, 200 μM and 300 μM $ZnCl_2$. Data were recorded at 20 °C from 300 nm to 195 nm with a scanning speed of 50 nm/min. Three scans were performed with a step size of 0.5 nm and a bandwidth of 1 nm and averaged for each condition. The solvent background was subtracted from each spectrum for all the measurements. The secondary structure composition was calculated using the CDNN package [56].

4.4. Fluorescence spectroscopy

The measurements were carried out at 20 °C utilizing a Fluorolog-3 spectrofluorometer (Horiba Jobin Yvon Inc.). Fluorescence spectra of Trp residues were recorded for 2 μM Nucb2s in buffer C either in the presence of 5 mM EDTA or 10 mM $MgCl_2$ and 100 μM, 200 μM and 300 μM $ZnCl_2$. Both homologues were incubated in the appropriate solution for 30 min before the measurement. The spectra were recorded between 310 and 500 nm, with an excitation wavelength of 295 nm. The obtained spectra were corrected for buffer contribution.

4.5. Sedimentation velocity analytical centrifugation (SV-AUC)

Nucb2 samples were subjected to AUC in the absence and presence of different metal cations. Sedimentation velocity experiments were performed at 20 °C and 50,000 rpm on a Beckman Coulter Proteome Lab XL-I ultracentrifuge (Beckman Coulter Inc.) equipped with an An-60Ti rotor. Protein samples (0.50 mg/ml, 0.75 mg/ml and 1.0 mg/ml) were prepared in buffer C supplemented with either 5 mM EDTA, 10 mM $MgCl_2$ or 100 μM, 200 μM or 300 μM $ZnCl_2$. The wavelength used for sample detection was 280 nm. The protein partial specific volumes (0.727 ml/g and 0.732 ml/g for ggNucb2 and hsNucb2, respectively), buffer density (1.0059 g/ml, 1.0057 g/ml and 1.0060 g/ml for EDTA-, $MgCl_2$- or $ZnCl_2$-containing buffer, respectively) and viscosity (1.0265 mPa × s, 1.0258 mPa × s and 1.0228 mPa × s for EDTA-, $MgCl_2$- or $ZnCl_2$-containing buffer, respectively) were calculated with SEDNTERP [108]. Time-corrected data were analysed with Sedfit software (version 16.1) using the built-in continuous sedimentation coefficient distribution model c(s). Maximum-entropy regularization of the c(s) model was set to a confidence level of 0.68 [109,110].

4.6. Hydrogen-deuterium exchange coupled with mass spectrometry (HDX-MS)

The HDX-MS experiments were performed as described previously [49], but to obtain the highest sequence coverage, the Nepenthesin-2 enzyme was used instead of pepsin for online protein digestion, utilizing a 2.1 mm × 20 mm Nepenthesin-2 column (AffiPro). HDX-MS was performed for both Nucb2s in the presence of 5 mM EDTA, 10 mM $MgCl_2$ and 100 μM $ZnCl_2$. Fifteen microlitres of ggNucb2 or hsNucb2 (95 μM of each) was diluted with 35 μl of buffer C (H_2O-based) in the absence and presence of the appropriate additive. The proteins were acidified by mixing with 10 μl of H_2O-based quench buffer containing 2 M glycine, pH 2.5. Proteins were digested online with a 2.1 mm × 20 mm Nepenthesin-2 column (AffiPro) at 20 °C. The generated peptides were trapped on a VanGuard precolumn (C18, 2.1 mm × 5 mm; Waters) and desalted for 1.5 min at a flow rate of 120 μl/min of solvent A (0.07% formic acid in Milli-Q water) controlled by the nanoACQUITY Auxilary Solvent Manager. Subsequently, peptides were resolved by a reverse-phase column ACQUITY UPLC BEH C18 column (2.1 mm × 50 mm, Waters) using a 6–40% gradient of acetonitrile in 0.01% formic acid at a flow rate of 90 μl/min, controlled by the nanoACQUITY Binary Solvent Manager.

4.7. Isothermal titration calorimetry (ITC)

The binding of Ca^{2+}, Zn^{2+} and Mg^{2+} to Nucb2s was monitored using a Nano-ITC calorimeter (TA Waters, USA) at 25 °C with a cell volume of 1 ml. All experiments were performed in buffer D. The Nucb2 (titrate) concentration was 0.032–0.075 mM, whereas the metal ion (titrant) concentration was 1–6 mM. Concentrations of titrate and titrant were adjusted to obtain the best isotherms for proper analysis of equilibria and to highlight different processes throughout the titration experiment. After temperature equilibration, successive injections of the titrant were made into the reaction cell in 5.22-μl increments at 300-s intervals with stirring at 250 rpm. Control experiments to determine the heats of titrant dilution were performed using identical injections of Ca^{2+}/Zn^{2+}/Mg^{2+} in the absence of protein. The net reaction heat was obtained by subtracting the dilution heat from the corresponding total heat of reaction.

The titration data were analysed using NanoAnalyze (version 3.3.0), NITPIC (version 1.2.7) [111,112] and SEDPHAT (version 15.2b) [113]. First, data were preprocessed using NanoAnalyze software dedicated to the Nano-ITC calorimeter. Second, data integration and baseline subtraction were conducted using NITPIC freeware. Afterwards, integrated data were fitted with SEDPHAT. Depending on the analysed variant, different models of interaction were used for fitting; however, all of the variants titrated with Ca^{2+}, as well as hsNucb2 titrated with Zn^{2+}, gave good fits for the standard ABB model, where a unit of protein possesses two symmetrical binding sites: $A + B + B \rightleftharpoons AB + B \rightleftharpoons ABB$ [113]. Another model that was used was one that takes into account the self-association of monomers into dimers that coincides with metal ion binding: $(A + A) + B + B \rightleftharpoons AB + A + B \rightleftharpoons (AA)B + B \rightleftharpoons (AA)BB$. The model was used to simulate the first tendency to gradually increase the exothermic process that was visible mostly for ggNucb2 titrated with Ca^{2+} but was very discrete for hsNucb2 samples. Last, Nucb2s titrated with Mg^{2+} were best fitted with a simple $A + B \rightleftharpoons AB$ model, which suggests that hsNucb2 and ggNucb2 bind only one Mg^{2+} ion. Data were fitted first with constrained values obtained from prefitting in NanoAnalyze and subsequently revised in SEDPHAT with floating parameters of an incompetent fraction of protein and $\log K_x$ with the corresponding ΔH_x under the appropriate model of interaction. The error estimates for the fitting results were produced using Monte Carlo analysis, individually for each experiment, with

500 iterations and a 0.9 level of confidence. For hsNucb2 samples titrated with Ca^{2+} and Zn^{2+}, single isotherms fitted to the ABB model gave good and reproducible results, but ggNucb2 samples titrated with Ca^{2+} gave significantly more complex results and were analysed using three different approaches: i) "narrow range" fit that focuses on the second isotherm alone and ii) "broad range" fit that fits both processes observable throughout the titration.

4.8. Small-angle X-ray scattering (SAXS)

SAXS profiles for both Nucb2s in solution were obtained by the use of XEUSS 2.0 SAXS/WAXS system (Xenocs, Grenoble, France). The ggNucb2 and hsNucb2 samples (protein concentration of 3.5 mg/ml) with 5 mM EDTA or 10 mM Ca^{2+}, 100 μM Zn^{2+} and 10 mM Mg^{2+} and reference sample (BSA, bovine serum albumin) were injected into the flow cell and exposed to X-ray radiation (gallium Kα emission of 9.2 keV) produced by a MetalJet D2 microfocus generator (Excillum AB, Kista, Sweden). For each sample, 10 independent frames (exposure time 600 s per frame) were recorded using a PILATUS3 1 M detector (DECTRIS Ltd., Baden-Daettwil, Switzerland). Scattering data for ggNucb2 and hsNucb2 were integrated using Foxtrot [114] and processed using the SAS data analysis module from the ATSAS package [115].

4.9. Transmission electron microscopy (TEM)

Microscopic observations were performed using a Hitachi H-800 conventional transmission electron microscope (Hitachi Hightech, Japan). An accelerating voltage of 150 kV and the EMSIS Quemesa CCD camera were used. The samples were prepared similar to protocols [116,117]. Commercial carbon on a copper mesh 200 grid (AGS160) was used (Agar Scientific, United Kingdom). Before each experiment, Nucb2s (150 μM) in buffer C were incubated with 300 μM Zn^{2+}, 10 mM Ca^{2+} and 10 mM Mg^{2+} at 4 °C for two weeks. Subsequently, 20 μl of the Nucb2s were applied on a strip of parafilm or a silicone pad, and 150 μl of deionized water was added. The grid was placed on a drop of sample for adhesion, and after 30 s, it was blotted on filter paper. The grid was immediately transferred for water droplets for 60 s on each of them. After removing the last portion of water, the sample was blotted with filter paper and immediately covered with 4 μl of 2% uranyl acetate. After 30 s of staining, the grid was blotted and allowed to dry in an ajar petri dish for at least 24 h. The same protocol was used to determine the morphology of the supernatant and precipitate of ggNucb2 upon the addition of 300 μM Zn^{2+} after the AUC experiment.

At the preparation stage, we compared usage of the carbon films straight out of the box and glow-discharged, different protein concentrations, sample washing with buffer and water as well as staining with uranyl acetate and uranyl formate. We are aware that the use of water as a medium for the long-term removal of excess concentrated proteins may cause changes in its structure, just as the use of non-glow-discharged grids may cause excessive protein complexation. For this reason, we note that the procedure used is only comparative and shows the tendency to produce protein complexes in the specific buffers.

Multidisciplinary Laboratory of Functional Nanomaterials (POIGT.02.02.00-00-025/09-00).

CRediT authorship contribution statement

Dominika Bystranowska: Investigation, Methodology, Project administration, Writing - original draft, Writing - review & editing. **Anna Skorupska:** Investigation, Methodology, Writing - original draft, Writing - review & editing. **Katarzyna Sołtys:** Investigation, Methodology, Writing - review & editing. **Michał Padjasek:** Investigation, Methodology, Writing - original draft, Writing - review & editing. **Artur Krężel:** Methodology, Writing - review & editing. **Andrzej Żak:** Investigation, Methodology, Writing - original draft, Writing - review & editing. **Magdalena Kaus-Drobek:** Investigation, Methodology, Writing - review & editing. **Michał Taube:** Investigation, Methodology, Writing - review & editing. **Maciej Kozak:** Methodology, Writing - review & editing. **Andrzej Ożyhar:** Methodology, Funding acquisition, Project administration, Supervision, Writing - original draft, Writing - review & editing.

Declaration of Competing Interest

The authors declare that they have no known competing financial interests or personal relationships that could have appeared to influence the work reported in this paper.

Appendix A. Supplementary data

Supplementary data to this article can be found online at https://doi.org/10.1016/j.csbj.2021.07.036.

References

[1] Bauer MC, Nilsson H, Thulin E, Frohm B, Malm J, Linse S. Zn^{2+} binding to human calbindin D 28k and the role of histidine residues. Protein Sci 2008;17:760–7. https://doi.org/10.1110/ps.073381108.

[2] Zhou Y, Xue S, Yang JJ. Integrative studies of Ca2+-binding proteins and their interactomes in biological systems. Metallomics. NIH Public Access 2013;5:29–42. https://doi.org/10.1039/C2MT20009K.

[3] McCall KA, Huang C, Fierke CA. Function and Mechanism of Zinc Metalloenzymes. J Nutr 2000;130:1437S–46S. https://doi.org/10.1093/jn/130.5.1437S.

[4] Ebel H, Günther T. Magnesium metabolism: a review. Clin Chem Lab Med 1980;18:257–70. https://doi.org/10.1515/cclm.1980.18.5.257.

[5] Clapham DE. Calcium signaling. Cell 2007;131:1047–58. https://doi.org/10.1016/j.cell.2007.11.028.

[6] Ikura M. Calcium binding and conformational response in EF-hand proteins. Trends Biochem Sci 1996;21:14–7. https://doi.org/10.1016/S0968-0004(06)80021-6.

[7] Kretsinger RH, Nockolds CE. Carp muscle calcium-binding protein. II. Structure determination and general description. J Biol Chem 1973;248:3313–26.

[8] Romani A, Scarpa A. Regulation of cell magnesium. Arch Biochem Biophys 1992;298:1–12. https://doi.org/10.1016/0003-9861(92)90086-C.

[9] Malmendal A, Evenäs J, Thulin E, Gippert GP, Drakenberg T, Forsén S. When size is important: accommodation of magnesium in a calcium binding regulatory domain. J Biol Chem 1998;273:28994–9001. https://doi.org/10.1074/jbc.273.44.28994.

[10] Kochańczyk T, Drozd A, Krężel A. Relationship between the architecture of zinc coordination and zinc binding affinity in proteins - insights into zinc regulation. Metallomics. Royal Society of Chemistry 2015;7:244–57. https://doi.org/10.1039/C4MT00094C.

[11] Andreini C, Banci L, Bertini I, Rosato A. Counting the zinc-proteins encoded in the human genome. J Proteome Res 2006;5:196–201. https://doi.org/10.1021/pr050361j.

[12] Colvin RA, Holmes WR, Fontaine CP, Maret W. Cytosolic zinc buffering and muffling: their role in intracellular zinc homeostasis. Metallomics. Metallomics 2010;2:306. https://doi.org/10.1039/b926662c.

[13] Zheng H, Chruszcz M, Lasota P, Lebioda L, Minor W. Data mining of metal ion environments present in protein structures. J Inorg Biochem 2008;102:1765–76. https://doi.org/10.1016/j.jinorgbio.2008.05.006.

[14] Lee M, Gippert G, Soman K, Case D, Wright P. Three-dimensional solution structure of a single zinc finger DNA-binding domain. Science 1989;245 (4918):635–7. https://doi.org/10.1126/science:2503871.

[15] Auld DS. Structural Zinc Sites. Handbook of Metalloproteins. Chichester, UK: John Wiley & Sons, Ltd; 2006. doi:10.1002/0470028637.met014.

[16] Kluska K, Adamczyk J, Krężel A. Metal binding properties, stability and reactivity of zinc fingers. Coord Chem Rev. Elsevier B.V. 2018;367:18–64. https://doi.org/10.1016/j.ccr.2018.04.009.

[17] Andreini C, Banci L, Bertini I, Rosato A. Zinc through the three domains of life. J Proteome Res 2006;5:3173–8. https://doi.org/10.1021/pr0603699.

[18] Krężel A, Maret W. Zinc-buffering capacity of a eukaryotic cell at physiological pZn. J Biol Inorg Chem 2006;11:1049–62. https://doi.org/10.1007/s00775-006-0150-5.

[19] Fraker PJ, Telford WG. A reappraisal of the role of zinc in life and death decisions of cells. Proceedings of the Society for Experimental Biology and Medicine. Blackwell Publishing Inc.; 1997. pp. 229–236. doi:10.3181/00379727-215-44132.

[20] Clegg M, Hanna L, Niles B, Momma T, Keen C. Zinc deficiency-induced cell death. IUBMB Life (International Union Biochem Mol Biol Life) 2005;57:661–9. https://doi.org/10.1080/15216540500264554.

[21] Kimura T, Kambe T. The functions of metallothionein and ZIP and ZnT transporters: an overview and perspective. Int J Mol Sci. MDPI AG 2016;17:336. https://doi.org/10.3390/ijms17030336.

[22] Thomas RC, Coles JA, Deitmer JW. Homeostatic muffling [9]. Nature 1991:564. https://doi.org/10.1038/350564b0.

[23] Frederickson CJ, Suh SW, Silva D, Frederickson CJ, Thompson RB. Importance of zinc in the central nervous system: The zinc-containing neuron. J Nutr. American Institute of Nutrition; 2000. doi:10.1093/jn/130.5.1471s.

[24] Foster MC, Leapman RD, Li MX, Atwater I. Elemental composition of secretory granules in pancreatic islets of Langerhans. Biophys J 1993;64:525–32. https://doi.org/10.1016/S0006-3495(93)81397-3.

[25] Maret W. Metals on the move: Zinc ions in cellular regulation and in the coordination dynamics of zinc proteins. Biometals 2011;24:411–8. https://doi.org/10.1007/s10534-010-9406-1.

[26] Maret W. Zinc biochemistry: from a single zinc enzyme to a key element of life. Adv Nutr 2013;4:82–91. https://doi.org/10.3945/an.112.003038.

[27] Ayton S, Lei P, Bush AI. Metallostasis in Alzheimer's disease. Free Radical Biology and Medicine. Elsevier Inc.; 2013. pp. 76–89. doi:10.1016/j.freeradbiomed.2012.10.558.

[28] McLoughlin IJ, Hodge JS. Zinc in depressive disorder. Acta Psychiatr Scand 1990;82:451–3. https://doi.org/10.1111/j.1600-0447.1990.tb03077.x.

[29] Zhang T, Pauly T, Nagel-Steger L. Stoichiometric Zn^{2+} interferes with the self-association of Aβ42: Insights from size distribution analysis. Int J Biol Macromol 2018;113:631–9. https://doi.org/10.1016/J.IJBIOMAC.2018.02.123.

[30] Solomonov I, Korkotian E, Born B, Feldman Y, Bitler A, Rahimi F, et al. Zn^{2+}-Aβ40 complexes form metastable quasi-spherical oligomers that are cytotoxic to cultured hippocampal neurons. J Biol Chem 2012;287:20555–64. https://doi.org/10.1074/jbc.M112.344036.

[31] Roman AY, Devred F, Byrne D, La Rocca R, Ninkina NN, Peyrot V, et al. Zinc induces temperature-dependent reversible self-assembly of tau. J Mol Biol 2019;431:687–95. https://doi.org/10.1016/j.jmb.2018.12.008.

[32] Brender JR, Hartman K, Nanga RPR, Popovych N, de la Salud Bea R, Vivekanandan S, et al. Role of zinc in human islet amyloid polypeptide aggregation. J Am Chem Soc 2010;132:8973–83. https://doi.org/10.1021/ja1007867.

[33] Salamekh S, Brender JR, Hyung S-J, Nanga RPR, Vivekanandan S, Ruotolo BT, et al. A two-site mechanism for the inhibition of IAPP amyloidogenesis by zinc. J Mol Biol 2011;410:294–306. https://doi.org/10.1016/j.jmb.2011.05.015.

[34] Calabrese MF, Miranker AD. Metal binding sheds light on mechanisms of amyloid assembly. Prion. Prion 2009;3:1–4. https://doi.org/10.4161/pri.3.1.8601.

[35] Valentine JS, Doucette PA, Zittin Potter S. Copper-zinc superoxide dismutase and amyotrophic lateral sclerosis. Annu Rev Biochem 2005;74:563–93. https://doi.org/10.1146/annurev.biochem.72.121801.161647.

[36] Noy D, Solomonov I, Sinkevich O, Arad T, Kjaer K, Sagi I. Zinc-amyloid β interactions on a millisecond time-scale stabilize non-fibrillar Alzheimer-related species. J Am Chem Soc 2008;130:1376–83. https://doi.org/10.1021/ja076282l.

[37] Barnikol-Watanabe S, Groß NA, Götz H, Henkel T, Karabinos A, Kratzin H, et al. Human protein NEFA, a novel DNA binding/EF-hand/leucine zipper protein. Molecular cloning and sequence analysis of the cDNA, isolation and characterization of the protein. Biol Chem Hoppe Seyler 1994;375:497–512.

[38] Oh-I S, Shimizu H, Satoh T, Okada S, Adachi S, Inoue K, et al. Identification of nesfatin-1 as a satiety molecule in the hypothalamus. Nature 2006;443:709–12. https://doi.org/10.1038/nature05162.

[39] Ramanjaneya M, Chen J, Brown JE, Tripathi G, Hallschmid M, Patel S, et al. Identification of nesfatin-1 in human and murine adipose tissue: a novel depot-specific adipokine with increased levels in obesity. Endocrinology 2010. https://doi.org/10.1210/en.2009-1358.

[40] Rose-Martel M, Smiley S, Hincke MT. Novel identification of matrix proteins involved in calcitic biomineralization. J Proteomics 2015;116:81–96. https://doi.org/10.1016/j.jprot.2015.01.002.

[41] Kan JY, Yen MC, Wang JY, Wu DC, Chiu YJ, Ho YW, et al. Nesfatin-1/Nucleobindin-2 enhances cell migration, invasion, and epithelial-mesenchymal transition via LKB1/AMPK/TORC1/ZEB1 pathways in colon cancer. Oncotarget 2016;7:31336–49. https://doi.org/10.18632/oncotarget.9140.

[42] Ramanjaneya M, Tan BK, Rucinski M, Kawan M, Hu J, Kaur J, et al. Nesfatin-1 inhibits proliferation and enhances apoptosis of human adrenocortical H295R cells. J Endocrinol 2015. https://doi.org/10.1530/JOE-14-0496.

[43] Zhang AQ, Li XL, Jiang CY, Lin L, Shi RH, De CJ, et al. Expression of nesfatin-1/NUCB2 in rodent digestive system. World J Gastroenterol 2010. https://doi.org/10.3748/wjg.v16.i14.1735.

[44] Garcia-Galiano D, Pineda R, Ilhan T, Castellano JM, Ruiz-Pino F, Sanchez-Garrido MA, et al. Cellular distribution, regulated expression, and functional role of the anorexigenic peptide, NUCB2/nesfatin-1, in the testis. Endocrinology 2012;153:1959–71. https://doi.org/10.1210/en.2011-2032.

[45] Foo KS, Brauner H, Östenson CG, Broberger C. Nucleobindin-2/nesfatin in the endocrine pancreas: distribution and relationship to glycaemic state. J Endocrinol 2010. https://doi.org/10.1677/JOE-09-0254.

[46] Gonzalez R, Tiwari A, Unniappan S. Pancreatic beta cells colocalize insulin and pronesfatin immunoreactivity in rodents. Biochem Biophys Res Commun 2009;381:643–8. https://doi.org/10.1016/j.bbrc.2009.02.104.

[47] Sun S, Yang H. Tissue-specific localization NUCB2/nesfatin-1 in the liver and heart of mouse fetus. Dev Reprod 2018;22:331–9. https://doi.org/10.12717/DR.2018.22.4.331.

[48] Kanuru M, Raman R, Aradhyam GK. Serine protease activity of calnuc: regulation by Zn^{2+} and G proteins. J Biol Chem 2013;288:1762–73. https://doi.org/10.1074/jbc.M112.382846.

[49] Skorupska A, Bystranowska D, Dąbrowska K, Ożyhar A. Calcium ions modulate the structure of the intrinsically disordered Nucleobindin-2 protein. Int J Biol Macromol 2020;154:1091–104. https://doi.org/10.1016/J.IJBIOMAC.2020.03.110.

[50] White RE, Hartzell HC. Magnesium ions in cardiac function. Regulator of ion channels and second messengers. Biochem Pharmacol 1989;38:859–67. https://doi.org/10.1016/0006-2952(89)90272-4.

[51] Cole TB, Wenzel HJ, Kafer KE, Schwartzkroin PA, Palmiter RD. Elimination of zinc from synaptic vesicles in the intact mouse brain by disruption of the ZnT3 gene. Proc Natl Acad Sci U S A 1999;96:1716–21. https://doi.org/10.1073/pnas.96.4.1716.

[52] Zalewski PD, Millard SH, Forbes IJ, Kapaniris O, Slavotinek A, Betts WH, et al. Video image analysis of labile zinc in viable pancreatic islet cells using a specific fluorescent probe for zinc. J Histochem Cytochem 1994;42:877–84. https://doi.org/10.1177/42.7.8014471.

[53] Eichelsdoerfer JL, Evans JA, Slaugenhaupt SA, Cuajungco MP. Zinc dyshomeostasis is linked with the loss of mucolipidosis IV-associated TRPML1 ion channel. J Biol Chem 2010;285:34304–8. https://doi.org/10.1074/jbc.C110.165480.

[54] Chung H, Yoon YH, Hwang JJ, Cho KS, Koh JY, Kim J-G. Ethambutol-induced toxicity is mediated by zinc and lysosomal membrane permeabilization in cultured retinal cells. Toxicol Appl Pharmacol 2009;235:163–70. https://doi.org/10.1016/j.taap.2008.11.006.

[55] Kelly S, Price N. The use of circular dichroism in the investigation of protein structure and function. Curr Protein Pept Sci 2005. https://doi.org/10.2174/1389203003381315.

[56] Böhm G, Muhr R, Jaenicke R. Quantitative analysis of protein far UV circular dichroism spectra by neural networks. Protein Eng 1992;5:191–5. https://doi.org/10.1093/protein/5.3.191.

[57] Permyakov EA, Uversky VN. Fluorescence spectroscopy of intrinsically disordered proteins. instrumental analysis of intrinsically disordered proteins. Hoboken, NJ, USA: John Wiley & Sons, Inc; 2010. p. 323–44. https://doi.org/10.1002/9780470602614.ch11.

[58] Islam A, Adamik B, Hawari FI, Ma Ge, Rouhani FN, Zhang J, et al. Extracellular TNFR1 release requires the calcium-dependent formation of a nucleobindin 2-ARTS-1 complex. J Biol Chem 2006;281:6860–73. https://doi.org/10.1074/jbc.M509397200.

[59] Taniguchi N, Taniura H, Niinobe M, Takayama C, Tominaga-Yoshino K, Ogura A, et al. The postmitotic growth suppressor necdin interacts with a calcium-binding protein (NEFA) in neuronal cytoplasm. J Biol Chem 2000;275:31674–81. https://doi.org/10.1074/jbc.M005103200.

[60] Romani AMP. Cellular magnesium homeostasis. Arch Biochem Biophys. NIH Public Access 2011;512:1–23. https://doi.org/10.1016/j.abb.2011.05.010.

[61] Englander SW, Sosnick TR, Englander JJ, Mayne L. Mechanisms and uses of hydrogen exchange. Curr Opin Struct Biol 1996;6:18–23. https://doi.org/10.1016/S0959-440X(96)80090-X.

[62] Zhang Z, Smith DL. Determination of amide hydrogen exchange by mass spectrometry: a new tool for protein structure elucidation. Protein Sci 1993;2:522–31. https://doi.org/10.1002/pro.5560020404.

[63] Wales TE, Engen JR. Hydrogen exchange mass spectrometry for the analysis of protein dynamics. Mass Spectrom Rev 2006;25:158–70. https://doi.org/10.1002/(ISSN)1098-278710.1002/mas.v25:110.1002/mas.20064.

[64] Konermann L, Pan J, Liu Y-H. Hydrogen exchange mass spectrometry for studying protein structure and dynamics. Chem Soc Rev 2011;40:1224–34. https://doi.org/10.1039/C0CS00113A.

[65] Engen JR. Analysis of protein conformation and dynamics by hydrogen/deuterium exchange MS. Anal Chem 2009;81:7870–5. https://doi.org/10.1021/ac901154s.

[66] Kikhney AG, Svergun DI. A practical guide to small angle X-ray scattering (SAXS) of flexible and intrinsically disordered proteins. FEBS Lett. Elsevier B.V. 2015:2570–7. https://doi.org/10.1016/j.febslet.2015.08.027.

[67] Svergun DI, Koch MHJ. Small-angle scattering studies of biological macromolecules in solution. Reports Prog Phys 2003;66:1735–82. https://doi.org/10.1088/0034-4885/66/10/R05.

[68] Bernadó P, Svergun DI. Structural analysis of intrinsically disordered proteins by small-angle X-ray scattering. Mol BioSystems. The Royal Society of Chemistry 2012;8:151–67. https://doi.org/10.1039/C1MB05275F.

[69] Receveur-Brechot V, Durand D. How random are intrinsically disordered proteins? A small angle scattering perspective. Curr Protein Pept Sci 2012;13:55–75. https://doi.org/10.2174/138920312799277901.

[70] Cordeiro TN, Herranz-Trillo F, Urbanek A, Estaña A, Cortés J, Sibille N, et al. Structural characterization of highly flexible proteins by small-angle scattering. In: Advances in experimental medicine and biology. New York LLC: Springer; 2017. p. 107–29. https://doi.org/10.1007/978-981-10-6038-0_7.

[71] La GA. diffraction des rayons X aux très petits angles: application à l'étude de phénomènes ultramicroscopiques. Ann Phys (Paris) 1939;11:161–237. https://doi.org/10.1051/anphys/193911120161.

[72] Svergun DI. Determination of the regularization parameter in indirect-transform methods using perceptual criteria. J Appl Crystallogr 1992;25:495–503. https://doi.org/10.1107/S0021889892001663.

[73] Arias-Moreno X, Abian O, Vega S, Sancho J, Velazquez-Campoy A. Protein-cation interactions: structural and thermodynamic aspects. Curr Protein Pept Sci 2011;12:325–38. https://doi.org/10.2174/138920311795906664.

[74] Won H-S, Low LY, De Guzman R, Martinez-Yamout M, Jakob U, Jane Dyson H. The Zinc-dependent redox switch domain of the chaperone Hsp33 has a novel fold. J Mol Biol 2004;341:893–9. https://doi.org/10.1016/j.jmb.2004.06.046.

[75] Sotomayor-Perez AC, Ladant D, Chenal A. Disorder-to-order transition in the CyaA toxin RTX domain: implications for toxin secretion. Toxins (Basel) 2014;7:1–20. https://doi.org/10.3390/toxins7010001.

[76] Hodkinson JP, Radford SE, Ashcroft AE. The role of conformational flexibility in β 2-microglobulin amyloid fibril formation at neutral pH. Rapid Commun Mass Spectrom 2012;26:1783–92. https://doi.org/10.1002/rcm.6282.

[77] Zahid H, Miah L, Lau AM, Brochard L, Hati D, Bui TTT, et al. Zinc-induced oligomerization of zinc α2 glycoprotein reveals multiple fatty acid-binding sites. Biochem J 2016;473:43–54. https://doi.org/10.1042/BJ20150836.

[78] Li RH, Liu GB, Wang H, Zheng YZ. Effects of Fe3+ and zn2+ on the structural and thermodynamic properties of a soybean ASR protein. Biosci Biotechnol Biochem 2013;77:475–81. https://doi.org/10.1271/bbb.120666.

[79] Bannister WH. The biological chemistry of the elements: the inorganic chemistry of life. Biochem Educ 1992;20:62–3. https://doi.org/10.1016/0307-4412(92)90039-O.

[80] Mónico A, Zorrilla S, Rivas G, Pérez-Sala D. Zinc differentially modulates the assembly of soluble and polymerized vimentin. Int J Mol Sci 2020;21:2426. https://doi.org/10.3390/ijms21072426.

[81] Ivaska J, Pallari HM, Nevo J, Eriksson JE. Novel functions of vimentin in cell adhesion, migration, and signaling. Exp Cell Res. Academic Press Inc.; 2007. pp. 2050–2062. doi:10.1016/j.yexcr.2007.03.040

[82] Paramio JM, Jorcano JL. Beyond structure: Do intermediate filaments modulate cell signalling? BioEssays 2002;24:836–44. https://doi.org/10.1002/bies.10140.

[83] Eckes B, Dogic D, Colucci-Guyon E, Wang N, Maniotis A, Ingber D, et al. Impaired mechanical stability, migration and contractile capacity in vimentin-deficient fibroblasts. J Cell Sci 1998;111(Pt 1):1897–907.

[84] Mendez MG, Kojima S, Goldman RD. Vimentin induces changes in cell shape, motility, and adhesion during the epithelial to mesenchymal transition. FASEB J 2010;24:1838–51. https://doi.org/10.1096/fj.09-151639.

[85] Satelli A, Li S. Vimentin in cancer and its potential as a molecular target for cancer therapy. Cell Mol Life Sci 2011;68:3033–46. https://doi.org/10.1007/s00018-011-0735-1.

[86] Huo X, Wang H, Huo B, Wang L, Yang K, Wang J, et al. FTX contributes to cell proliferation and migration in lung adenocarcinoma via targeting miR-335-5p/NUCB2 axis. Cancer Cell Int 2020;20. https://doi.org/10.1186/s12935-020-1130-5.

[87] Naranjo JR, Sharma Y, Dizhoor A, Yu Zernii E, AYu R, Jr ZA, et al. Functional status of neuronal calcium sensor-1 is modulated by zinc binding. 2018. doi:10.3389/fnmol.2018.00459.

[88] Carpenter MC, Wilcox DE. Thermodynamics of formation of the insulin hexamer: metal-stabilized proton-coupled assembly of quaternary structure. Biochemistry 2014;53:1296–301. https://doi.org/10.1021/bi4016567.

[89] Frederickson CJ. Neurobiology of zinc and zinc-containing neurons. Int Rev Neurobiol 1989;31:145–238. https://doi.org/10.1016/S0074-7742(08)60279-2.

[90] Gower-Winter SD, Levenson CW. Zinc in the central nervous system: from molecules to behavior. BioFactors. NIH Public Access 2012;38:186–93. https://doi.org/10.1002/biof.1012.

[91] Szewczyk B. Zinc homeostasis and neurodegenerative disorders. Front Aging Neurosci. Frontiers Media SA 2013. https://doi.org/10.3389/fnagi.2013.00033.

[92] Faller P, Hureau C, Berthoumieu O. Role of metal ions in the self-assembly of the Alzheimer's amyloid-β peptide. Inorg Chem 2013;52:12193–206. https://doi.org/10.1021/ic4003059.

[93] Michel TM, Thome J, Martin D, Nara K, Zwerina S, Tatschner T, et al. Cu, Zn-And Mn-superoxide dismutase levels in brains of patients with schizophrenic psychosis. J Neural Transm 2004;111. https://doi.org/10.1007/s00702-004-0160-9.

[94] Li YV. Zinc and insulin in pancreatic beta-cells. Endocrine. Springer 2014;45:178–89. https://doi.org/10.1007/s12020-013-0032-x.

[95] Milthorpe BK, Nichol LW, Jeffrey PD. The polymerization pattern of zinc(II)-insulin at pH 7.0. BBA - Protein Struct 1977;495:195–202. https://doi.org/10.1016/0005-2795(77)90376-2.

[96] Foo KS, Brismar H, Broberger C. Distribution and neuropeptide coexistence of nucleobindin-2 mRNA/nesfatin-like immunoreactivity in the rat CNS. Neuroscience 2008;156:563–79. https://doi.org/10.1016/j.neuroscience:2008.07.054.

[97] Yang Y, Zhang B, Nakata M, Nakae J, Mori M, Yada T. Islet β-cell-produced NUCB2/nesfatin-1 maintains insulin secretion and glycemia along with suppressing UCP-2 in β-cells. J Physiol Sci 2019;69:733–9. https://doi.org/10.1007/s12576-019-00689-2.

[98] French-Pacheco L, Cuevas-Velazquez CL, Rivillas-Acevedo L, Covarrubias AA, Amero C. Metal-binding polymorphism in late embryogenesis abundant protein AtLEA4-5, an intrinsically disordered protein. PeerJ. 2018;2018. doi:10.7717/peerj.4930.

[99] Kocyła A, Tran JB, Krężel A. Galvanization of protein-protein interactions in a dynamic zinc interactome. Trends Biochem Sci. Elsevier Ltd 2021;46:64–79. https://doi.org/10.1016/j.tibs.2020.08.011.

[100] Valencia CA, Cotten SW, Duan J, Liu R. Modulation of nucleobindin-1 and nucleobindin-2 by caspases. FEBS Lett 2008;582:286–90. doi:S0014-5793(07)01289-6.

[101] Yosten GLC, Samson WK. Nesfatin-1 exerts cardiovascular actions in brain: Possible interaction with the central melanocortin system. Am J Physiol - Regul Integr Comp Physiol 2009;297:R330–6. https://doi.org/10.1152/ajpregu.90867.2008.

[102] Hofmann T, Ahnis A, Elbelt U, Rose M, Klapp BF, Stengel A, et al. NUCB2/nesfatin-1 is associated with elevated levels of anxiety in anorexia nervosa. PLoS ONE 2015;10:e0132058. https://doi.org/10.1371/journal.pone.0132058.

[103] Conchillo-Solé O, de Groot NS, Avilés FX, Vendrell J, Daura X, Ventura S. AGGRESCAN: A server for the prediction and evaluation of "hot spots" of aggregation in polypeptides. BMC Bioinf 2007;8:1–17. https://doi.org/10.1186/1471-2105-8-65.

[104] Garbuzynskiy SO, Lobanov MY, Galzitskaya OV. FoldAmyloid: a method of prediction of amyloidogenic regions from protein sequence. Bioinformatics 2010;26:326–32. https://doi.org/10.1093/bioinformatics/btp691.

[105] Bonito-Oliva A, Barbash S, Sakmar TP, Graham WV. Nucleobindin 1 binds to multiple types of pre-fibrillar amyloid and inhibits fibrillization. Sci Rep 2017;7:42880. https://doi.org/10.1038/srep42880.

[106] Bonito-Oliva A, Schedin-Weiss S, Younesi SS, Tiiman A, Adura C, Paknejad N, et al. Conformation-specific antibodies against multiple amyloid protofibril species from a single amyloid immunogen. J Cell Mol Med 2019;23:2103–14. https://doi.org/10.1111/jcmm.14119.

[107] Gupta R, Kapoor N, Raleigh DP, Sakmar TP. Nucleobindin 1 caps human islet amyloid polypeptide protofibrils to prevent amyloid fibril formation. J Mol Biol 2012;421:378–89. https://doi.org/10.1016/j.jmb.2012.04.017.

[108] Laue T. M. Ridgeway T. M., Pelletier S. L. SBD. Computer-aided interpretation of analytical sedimentation data for proteins. Anal Ultracentrifugation Biochem Polym Sci. 1992.

[109] Schuck P. Size-distribution analysis of macromolecules by sedimentation velocity ultracentrifugation and Lamm equation modeling. Biophys J 2000;78:1606–19. https://doi.org/10.1016/S0006-3495(00)76713-0.

[110] Schuck P. Sedimentation analysis of noninteracting and self-associating solutes using numerical solutions to the Lamm equation. Biophys J 1998;75:1503–12. https://doi.org/10.1016/S0006-3495(98)74069-X.

[111] Keller S, Vargas C, Zhao H, Piszczek G, Brautigam CA, Schuck P. High-precision isothermal titration calorimetry with automated peak-shape analysis. Anal Chem 2012;84:5066–73. https://doi.org/10.1021/ac3007522.

[112] Scheuermann TH, Brautigam CA. High-precision, automated integration of multiple isothermal titration calorimetric thermograms: new features of NITPIC. Methods 2015;76:87–98. https://doi.org/10.1016/j.ymeth.2014.11.024.

[113] Houtman JCD, Brown PH, Bowden B, Yamaguchi H, Appella E, Samelson LE, et al. Studying multisite binary and ternary protein interactions by global analysis of isothermal titration calorimetry data in SEDPHAT: application to adaptor protein complexes in cell signaling. Protein Sci 2007;16:30–42. https://doi.org/10.1110/ps.062558507.

[114] David G, Pérez J. Combined sampler robot and high-performance liquid chromatography: a fully automated system for biological small-angle X-ray scattering experiments at the Synchrotron SOLEIL SWING beamline. J Appl Crystallogr 2009;42:892–900. https://doi.org/10.1107/S0021889809029288.

[115] Manalastas-Cantos K, Konarev PV, Hajizadeh NR, Kikhney AG, Petoukhov MV, Molodenskiy DS, et al. ATSAS 3.0: expanded functionality and new tools for small-angle scattering data analysis. J Appl Crystallogr 2021;54:54. https://doi.org/10.1107/S1600576720013412.

[116] Scarff CA, Fuller MJG, Thompson RF, Iadaza MG. Variations on negative stain electron microscopy methods: Tools for tackling challenging systems. J Vis Exp 2018;2018. https://doi.org/10.3791/57199.

[117] Booth DS, Avila-Sakar A, Cheng Y. Visualizing proteins and macromolecular complexes by negative stain EM: from grid preparation to image acquisition. J Vis Exp 2011. https://doi.org/10.3791/3227.